

Report SDSMT/IAS/R-87/03

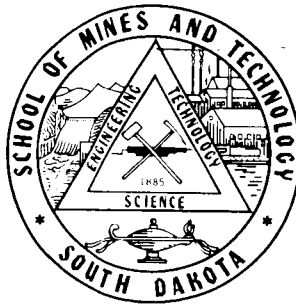
July 1987

RAIN VOLUME ESTIMATION OVER AREAS
USING SATELLITE AND RADAR DATABy: André A. Doneaud, T. H. Vonder Haar,
L. R. Johnson, P. Laybe, and D. Reinke

Prepared for:

Goddard Space Flight Center
NASA National Aeronautics
and Space Administration
600 Independence Ave., S.W.
Washington, DC 20546

Grant NAG 5-386

(NASA-CR-181115) RAIN VOLUME ESTIMATION
OVER AREAS USING SATELLITE AND RADAR DATA
Progress Report (South Dakota School of
Mines and Technology) 50 p Avail: NTIS HC
A03/MF A01

N87-26474

Unclas
CSCL 04B G3/47 0082688

Institute of Atmospheric Sciences

South Dakota School of Mines and Technology

Rapid City, South Dakota 57701-3995

Report SDSMT/IAS/R-87/03

July 1987

RAIN VOLUME ESTIMATION OVER AREAS
USING SATELLITE AND RADAR DATA

By: André A. Doneaud, T. H. Vonder Haar,¹
L. R. Johnson, P. Laybe,² and D. Reinke¹

Prepared for:

Goddard Space Flight Center
NASA National Aeronautics
and Space Administration
600 Independence Ave., S.W.
Washington, DC 20546

Grant NAG 5-386

¹Present Affiliation: Dept. of Atmospheric Sciences, Colorado
State University, Fort Collins, CO 80523.

²Present Affiliation: U.S. Army Atmospheric Science Laboratory,
White Sands Missile Range, NM 88002-5501.

ACKNOWLEDGMENTS

Support of this research was provided by the National Aeronautics and Space Administration (NASA) under Grant No. NAG-5-386. Thanks are given to Mr. Khan Md. Fakhruzzaman and Mr. Amos Makarau for helping in plotting some of the figures and to Mrs. Joie Robinson for work on the manuscript.

PRECEDING PAGE BLANK NOT FILMED

-iii-

PAGE ii INTENTIONALLY BLANK

TABLE OF CONTENTS

	<u>Page</u>
LIST OF FIGURES	vi
LIST OF TABLES	vii
1. INTRODUCTION AND BACKGROUND	1
2. DATA AND DATA PROCESSING	2
3. ANALYSIS OF THE DATA	9
3.1 Time Step Analysis	9
3.2 Cluster Lifetime Analysis	25
4. RESULTS	36
5. CONCLUDING REMARKS	39
6. PAPERS PRESENTED AND PUBLISHED	41
7. REFERENCES	42

PRECEDING PAGE BLANK NOT FILMED

LIST OF FIGURES

<u>Number</u>	<u>Title</u>	<u>Page</u>
1	Map showing the locations and the ranges (150 km) of the four 5.0 cm radars in western North Dakota and eastern Montana part of the NDCMP and the CCOPE (summer 1981)	3
2	Remapped infrared imagery (non-smoothed) for 12 June 1981	5
3	Remapped infrared imagery (smoothed) for 12 June 1981	5
4	Trends of radar echo area (A) and infrared temperature matching radar echo area (T_M) for the 18 analyzed clusters	11-13
5	Trends of radar maximum echo height (H), maximum reflectivity (Z), and temperature of infrared maximum count (T_{MX}) for the 18 analyzed clusters	15-17
6	Sequences of GOES Rapid Scan Satellite Images (IR and VIS) and radar reflectivity patterns for the 12 June, 2, 11, and 13 July clusters	19-23
7	Histograms of IR digital counts vs. satellite ATI's for the 18 cells	28-30
8	Scatter and linear regression of temperatures matching radar ATI and IR minimum temperature	32
9	Scatter and linear regression of temperatures matching radar ATI and average temperatures of IR maximum count	32
10	Scatter and linear regression of total rain volume versus ATI	33
11	Structures of radar reflectivities (A), and minimum temperature of IR digital counts (B), as functions of normalized area and time	35
12	Scatter and linear regression of ATI and average (over the cell duration) of IR minimum temperatures as determined by satellite imagery	38

LIST OF TABLES

<u>Number</u>	<u>Title</u>	<u>Page</u>
1	Characteristics of the Analyzed Clusters	8
2	Satellite ATI's as a function of digital counts and time for Cell 11 - 11 July 1981	10
3A	Characteristic Products of Bowman Radar and GOES Satellite Data for Six Clusters (or Cells) of Summer 1981	26
3B	Characteristic Products of Miles City Radar and GOES Satellite Data for Twelve Clusters (or Cells) of Summer 1981	27
4	Rain Volumes by Four Methods	37

1. INTRODUCTION AND BACKGROUND

The application of satellite data to a recently developed radar technique used to estimate convective rain volumes over areas is our primary concern. The Area-Time-Integral (ATI)* technique provides a means of estimating total rain volumes over fixed and floating target areas of the order of 1,000 to 100,000 km² for clusters lasting >40 min (Doneaud et al., 1981a, 1984a). The basis of the method is the existence of a strong correlation between the radar echo area coverage integrated over the lifetime of the storm and the radar estimated rain volume. The technique does not require consideration of the structure of echo intensities measured by radar or other means to generate rain volumes; only the area covered by radar echoes >25 dBz or by precipitation measured at the ground.

A variety of visible (VIS) and infrared (IR) methods for observing cloud properties and using them as predictor variables for rain volume estimation were developed in the last 15 years (Barrett and Martin, 1981). Some of these methods considered cloud histories in the calculation process (i.e., Griffith et al., 1976). Negri et al. (1984) found the Griffith-Woodley Technique (GWT) quite complicated, as it necessitates different conversion factors for each stage of cloud development for a given climate. The cited authors suggested a simplified version of the technique.

Griffith et al. (1981) showed that special precautions should be used to adjust the magnitude of the estimates when using the GWT technique in a much drier climate. Scofield and Oliver (1977) have developed a satellite rainfall estimation method for operational use in forecast offices primarily for flash flood prediction (large and long-lasting storms). Negri and Adler (1981) and Adler and Mach (1984) found cloud height-rainfall rate relations by considering only the period of maximum development of the convective system.

The ATI technique considers cloud histories and requires only one conversion factor to convert the ATI to total rain volume. The proposed method limits input to only satellite variables in estimating rain volumes. Relations between digital count thresholds which yield areas that match areas >25 dBz used to determine the ATI's have to be found to extend the technique. Other satellite quantities such as cloud top, minimum temperature, or thermodynamic profiles may also be useful to better understand selection processes that occur.

*The ATI is the product of the area covered by convective rain events (radar echoes >25 dBz or precipitation measured at the ground) and the time interval between radar scans or rain gage measurements, integrated over the lifetime of the convective event.

2. DATA AND DATA PROCESSING

Radar and GOES rapid scan satellite data were collected during the summer season of 1981. The radar data were collected in Bowman (southwestern North Dakota) as a part of the North Dakota Cloud Modification Project (NDCMP) and in Miles City (eastern Montana) as a part of the Cooperative Convective Precipitation Experiment (CCOPE), (Fig. 1). The rapid scan satellite data were collected as a part of CCOPE.

The radar data were processed at the South Dakota School of Mines and Technology. The Bowman and Miles City radars were Enterprise Electronics Corporation WR-100, 5.4-cm systems equipped with digital video integrator and processor and magnetic tape recorder. Data were recorded whenever there was convective activity within about a 150 km range at the Bowman site and between 10:00 a.m. and 10:00 p.m. local time at the Miles City site. One volume scan up to 15° elevation angle, using 1° increments, was recorded roughly every 10 min at Bowman and every 3 min (5 min) at Miles City. The first 20 km of range were blanked out to eliminate most of the ground clutter echoes. Radar receiver calibration data were recorded before and after each period of recording convective activity. The data tapes were processed following procedures similar to those described by Schroeder and Klazura (1978).

Only dBz values at low tilt angles defined as 1° elevation outside 50 km range, and 3° between 20 and 50 km are considered. Digital printouts of the dBz values at low tilt angle were prepared and converted from spherical to a rectangular coordinate system. From these products, individual radar echo clusters were identified by drawing a "box" around each cluster for each scan. These clusters are similar to the small mesoscale areas of Austin and Houze (1972), or the convective complexes described by Super and Heimbach (1980). The coordinates of the boxes were entered into a computer program that calculated the echo areas for the 25-dBz reflectivity threshold and the corresponding ATI's. The rain volume for each cluster was computed using an optimized Z-R relationship, $Z = 155 R^{1.88}$ (Smith et al., 1975). Details concerning the processing of the radar data can be found in Doneaud et al., 1984a).

Visible and Infrared Spin Scan Radiometer (VISSR) data from the GOES-East and GOES-West were used. The GOES-East and GOES-West are geostationary satellites (Clark, 1983) stationed at 75°W and 135°W, respectively. On a normal day, each transmits two images per hour of the entire disk of the earth in both the visible (0.55 μm -0.75 μm) and infrared (10.0 μm -12.5 μm) spectral wavelengths. During "Rapidscan," a smaller area is scanned and images are transmitted more frequently. High temporal frequency VISSR data were transmitted from GOES-West every 3 min during the CCOPE experiment. "Rapidscan" data for the 18 cases analyzed were used to match, as closely as possible, the satellite image times to radar scan times. All the images were from

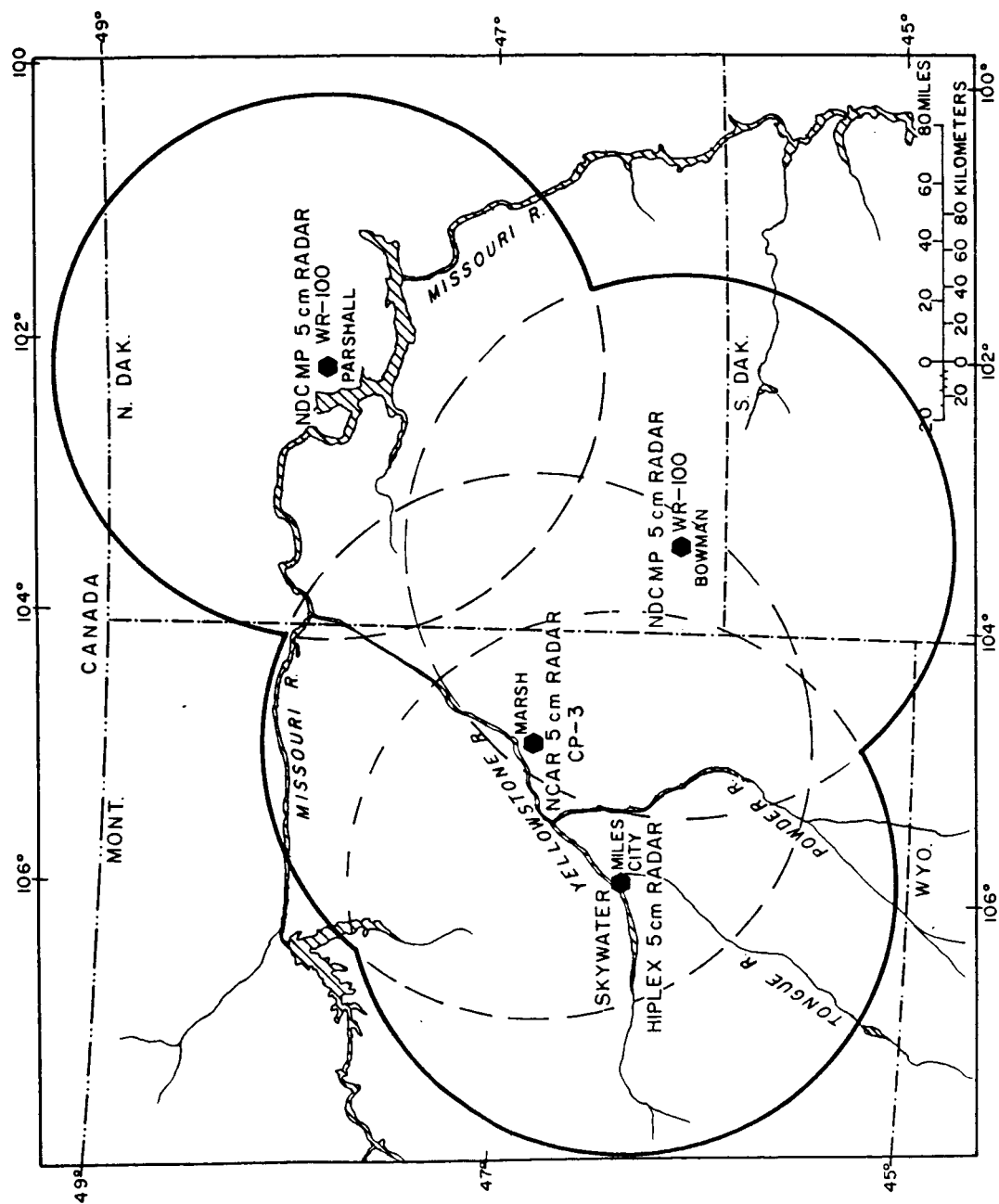


Fig. 1: Map showing the locations and the ranges (100 km) of the four 5.0 cm radars in western North Dakota and eastern Montana part of the NDCMP and the CCOPE (summer 1981).

GOES-West except for four images that were from GOES-East (1838, 1841, 1941 GMT on 12 June and 0335 GMT on 2 July). The use of the GOES-East data helped in following more closely the evolution of the clouds by reducing time gaps and making the data more continuous in nature.

Magnetic tapes of digital satellite data were acquired from the Bureau of Reclamation, the University of Wisconsin through the National Environmental Satellite Data Information Service (NESDIS), and the GOES data archive at CSU.

The satellite data were processed at the IRIS/DRSES (Interactive Research Imaging System/Direct Readout Satellite Earth Station) facility, located at CSU's Department of Atmospheric Science. The IRIS/DRSES (Laybe, 1983) is a combination of a real-time GOES collection system and satellite imaging system. The imaging system, IRIS, includes a collection of application programs for the manipulation of satellite data. Once the satellite data is processed into IRIS, the routines for 1) navigation; 2) remapping; and 3) smoothing of satellite images are performed.

The satellite imagery was remapped from the satellite coordinate system into a Lambert conformal projection so that the vertical and horizontal dimensions of an image pixel are nearly equal. The original image was "blown-up" to a higher resolution. The resultant resolution of the grid remapped satellite imagery is approximately 2.47 km². Thus, the remapped infrared satellite imagery appears very "blocky" because the original infrared resolution is 32 times larger than the resolution of the remapped infrared imagery.

The remapping routine divides the input image into discrete parts and relocates those parts according to the desired projection (Lambert conformal). Thus, the remapping routine can create sharp discontinuities of temperature between image pixels. An example of how this routine changes the satellite imagery can be seen by comparing Fig. 2 (non-smoothed) and Fig. 3 (smoothed). Smoothed images were used for visual photographic products. The non-smoothed images were used in the analysis.

The visible counts were normalized for solar zenith angle (Minnis and Harrison, 1984). The visible counts are related to energy by the relationship:

$$E = C^2 \quad , \quad (1)$$

where E is the energy and C is the visible count. The energy was normalized by the cosine of the solar zenith angle,

$$E_N = \frac{E}{\cos \xi} \quad , \quad (2)$$

ORIGINAL PAGE IS
OF POOR QUALITY

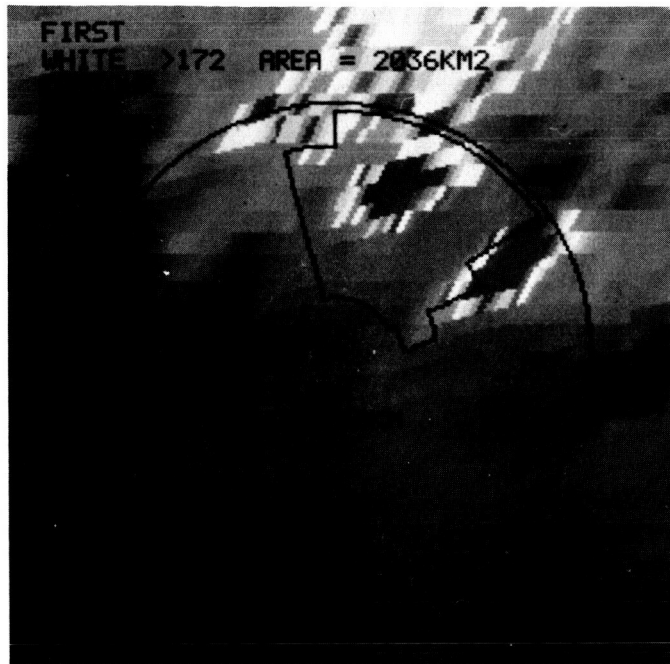


Fig. 2: Remapped infrared imagery (non-smoothed) for 12 June 1981.

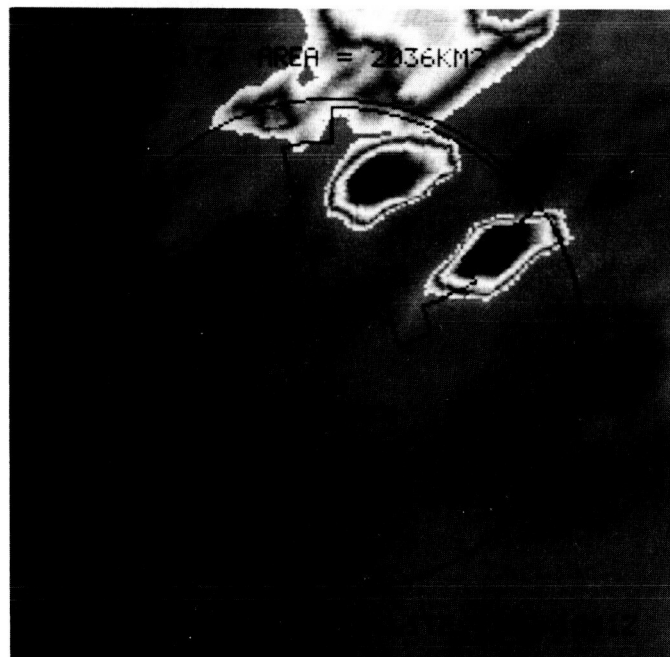


Fig. 3: Remapped infrared imagery (smoothed) for 12 June 1981.

where E_N is the normalized energy and ξ is the solar zenith angle. The normalized visible count is determined by taking the square root of the normalized energy,

$$C_N = \sqrt{E_N} \quad , \quad (3)$$

where C_N is the normalized visible count.

This normalization procedure was applied to the GOES-West visible data. The GOES-East visible data were normalized in the same fashion, with the exception that the right side of Eq. (1) was replaced by the term $(C-C_0)^2$, where $C_0 = 10$. This was necessary because the satellite data are uncalibrated. There is an observed difference in zero point between the two GOES (East and West) visible sensors. The value of C_0 was derived by comparing brightness histograms for both GOES-East and West visible data over the same geographical areas at approximately the same time. A fairly large area was used ($2 \times 10^4 \text{ km}^2$) to get a large number of data in the histogram calculation. The time difference between the GOES-East and West images was approximately 15 min. The infrared satellite detectors are stable between images and are calibrated to within $\pm 5^\circ$ at 295°K (Clark, 1983).

A radar sector of interest was defined to delineate specific radar echo clusters for each radar time throughout the radar echo cluster lifetime. The radar sector of interest was used to locate the convective cluster responsible for the rainfall in the remapped satellite data. The radar echo clusters within the defined sectors of interest were identified by drawing a "box" using axes and radials to encircle the cluster. The cluster echo areas of $>25 \text{ dBz}$ reflectivity threshold and the corresponding radar ATI and rain volume were calculated.

Next, a satellite sector of interest was defined by applying small adjustments to the radar sector using a manual processing technique. This was done to avoid including cloud features suspected of not being detected by the radar. It is one of the most delicate tasks of this investigation because of several considerations: a) satellite and radar systems respond to different characteristics of clouds at different atmospheric levels; b) time differences between satellite and radar data sets can vary by as much as 10 min; c) spatial positioning of the satellite observations relative to the radar location necessitates error inclusion due to limited accuracy of geometric corrections; d) vertical wind shear advects the cloud tops downwind from the location of the radar echo area; and e) in the definition of the matching satellite sector of interest, the inclusion or exclusion of cirrus spissatus debris is a very important decision. In this work, if the cirrus debris appeared to be completely detached horizontally from the radar echo cluster, the cirrus cloud cover was excluded from the satellite sector of interest.

To illustrate the processing technique used to define a satellite sector of interest by applying adjustments to a radar sector of interest, an example is discussed. As mentioned in the legend of Fig. 6(A-D), the dashed lines in the radar PPI's represent the radar sector of interest; the continuous lines in the IR satellite images are for the satellite sector of interest. The satellite sector of interest at 1759 GMT was reduced on the north side of cell 1A to avoid the inclusion of the northern cloud system (cirrus debris) into the computation. It will be seen later that this artifact generated substantial errors in the rain volume estimation (cell 1A). This system is not visible in the radar PPI (1801 GMT), except for a few weak cells located very close to the northern border of the radar sector of interest. A similar adjustment was made for the western border of the satellite sector of interest to avoid the inclusion in the computation clouds located on the western border of the satellite image. These clouds are not visible in the radar PPI. Adjustments were also made in a few other situations: In Fig. 6A at 1941 GMT (satellite time) north of cell 1A; in Fig. 6B at 0218 and 0241 GMT (satellite time) north of cell X2.

Eighteen clusters lasting 1-5 hours were analyzed for which both digital satellite and radar data existed. These storm events occurred in the Bowman radar area on 12 June and 2 July, and in the Miles City radar area on 11 July and 13 July. Table 1 describes some characteristic quantities of these clusters. The 12 June clusters occurred during the daytime, while the 2, 11, and 13 July clusters occurred during the nighttime. A total of 597 time steps of radar and 192 time steps of satellite images were analyzed. There were approximately 12-min time intervals between scans on the average at the Bowman site and 3-min (5-min) time intervals between scans at the Miles City site. The 3-min time intervals between scans recorded for 11 July and 13 July at the Miles City radar are responsible for the large difference between the number of images analyzed using radar and satellite data. The 12 June clusters were analyzed using both infrared and visible data. For the 2, 11, and 13 July clusters, only infrared data were available.

Table 1
Characteristics of the Analyzed Clusters

No.	Cluster Ident.	Date 1981	Time Period (Radar) (GMT)	Time Steps		Cluster Type	Satellite Data Type
				Radar	Satellite		
1	1A	12 June	1657 - 1955	14	13	Multicell	Infrared, Visible
2	1B	12 June	1746 - 1955	10	12	Multicell	Infrared, Visible
3	E	12 June	1657 - 1930	11	12	One Cell	Infrared, Visible
4	X1	2 July	0103 - 0453	19	16	Multicell	Infrared
5	X2	2 July	0201 - 0434	13	10	Multicell	Infrared
6	A	2 July	0103 - 0453	19	16	One Cell	Infrared
7	C1	11 July	0011 - 0329	66	9	Multicell	Infrared
8	C2	11 July	0138 - 0214	13	4	One Cell	Infrared
9	C3	11 July	0159 - 0311	24	5	One Cell	Infrared
10	C4	11 July	0129 - 0345	44	6	Multicell	Infrared
11	C5	11 July	0038 - 0450	73	13	Multicell	Infrared
12	C6	11 July	0159 - 0235	12	4	One Cell	Infrared
13	C7	11 July	0232 - 0450	35	9	One Cell	Infrared
14	C9	11 July	2102 - 0035	53	9	Multicell	Infrared
15	C10	11 July	2356 - 0217	48	7	Multicell	Infrared
16	C11	11 July	0129 - 0317	35	7	One Cell	Infrared
17	D1	13 July	2359 - 0346	59	20	Multicell	Infrared
18	D2	13 July	0041 - 0441	49	20	One Cell	Infrared

3. ANALYSIS OF THE DATA

3.1 Time Step Analysis

Using the technique described in Section 2, satellite digital counts above defined thresholds within the satellite sector of interest were counted and converted to area. Table 2 shows an example of digital counts versus area multiplied with the centered time interval between observations for cluster C11. The columns show the different time steps, while the rows are the product of area and time interval for a given IR digital count, column 1 (or temperature, column 10). Column 9 represents the ATI's (the sum of a row) for each threshold. Such tables were worked out for the 18 clusters or cells analyzed.

Histograms of area (multiplied by the centered time interval) versus digital count were produced for each satellite time step. For the lifetime of the storm, histograms were prepared of satellite ATI versus IR digital count (see Fig. 7A-S). These histograms and the computed radar area (multiplied by the centered radar time interval) were used to determine thresholds for satellite data that matched the radar area multiplied by time. This was performed by forcing the areas multiplied by time for satellite to be equal to that of radar. Both satellite and radar time series were reduced to a constant 15-min time increment by linear interpolation such that functional time dependence is comparable. The echo areas >25 dBz (multiplied by time), as well as the corresponding threshold count values, exhibit a large spectrum of variations during the storm's lifetime. No relationship was found between these variations and the stages of the storm's lifetime.

The trends of the echo areas (A) and of the temperature threshold (T_M) chosen to match the radar area are displayed in Figs. 4A-S for the 18 cells, respectively. For most of the long lasting cells, a visual inspection of these graphs emphasizes a general similarity of evolution and a tendency for satellite products to lag that of radar (Fig. 4A,B,E,G, and P). This can be seen by noting the near continuous high value of T_M during the latter half of the clusters' lifetime. A two-cycle oscillation emphasizing the multicell character of the clusters is demonstrated, except for Cells E, C2, C3, C4, C6, and C11. The effect of cirrus spissatus debris is evident in five of the cells, 1A (Fig. 4A), 1B (Fig. 4B), X2 (Fig. 4E), C4 (Fig. 4J), and C10 (Fig. 4O). The cirrus debris obscures the definition of the end and, sometimes, the beginning of a cluster (as a convective entity) from the satellite images. The effect of cirrus debris from a previous growing period is present in the satellite data trend (Fig. 4A), primarily because the initial stage of the cluster was overlaid by debris from the previous activity. Again, remnants of previous activity preclude initial observations in Fig. 4D (cluster X1), Fig. 4J (Cell C4), Fig. 4L (Cell C6), Fig. 4O (Cell C10), and Fig. 4S (Cell D2).

TABLE 2
Satellite ATI's for Cell 11 - 11 July 1981*

THR	0120	0141	0158	0215	0232	0235	0315	ATI	TEMP (C)
167	0.0	0.0	2.3	0.0	0.0	0.0	0.0	2.35	-26.5
166	0.0	0.0	2.3	0.0	0.0	0.0	0.0	2.35	-26.0
165	0.0	0.0	3.9	0.0	0.0	0.0	0.0	3.92	-25.5
164	0.0	0.0	7.1	0.0	0.0	0.0	0.0	7.06	-25.0
163	0.0	0.0	9.4	12.5	0.0	0.0	0.0	21.95	-24.5
162	0.0	11.1	14.1	29.0	0.0	0.0	0.0	54.19	-24.0
161	0.0	11.1	20.4	29.0	0.0	0.0	0.0	60.46	-23.5
160	0.0	24.9	22.7	66.6	0.0	0.0	0.0	114.29	-23.0
159	0.0	24.9	30.6	66.6	0.0	0.0	0.0	122.13	-22.5
158	0.0	24.9	37.6	66.6	0.0	0.0	0.0	129.19	-22.0
157	0.0	24.9	44.7	66.6	0.0	0.0	0.0	136.24	-21.5
156	0.0	40.2	52.5	66.6	0.5	0.0	0.0	159.78	-21.0
155	0.0	56.1	62.7	79.2	2.8	0.0	0.0	200.75	-20.5
154	0.0	56.1	68.2	79.2	5.1	0.0	0.0	208.55	-20.0
153	0.0	72.7	78.4	79.2	8.3	0.0	0.0	238.60	-19.5
152	0.0	72.7	87.0	79.2	12.0	0.0	0.0	250.92	-19.0
151	0.0	83.1	96.4	79.2	15.7	0.0	0.0	274.42	-18.5
150	0.0	143.4	110.5	127.0	20.4	2.0	0.0	403.20	-18.0
149	0.6	143.4	118.4	127.0	26.4	6.9	0.0	422.62	-17.5
148	2.7	164.1	129.4	127.0	33.3	21.8	0.0	478.28	-17.0
147	5.7	164.1	138.0	127.0	37.9	32.7	0.0	505.41	-16.5
146	11.4	175.9	141.9	127.0	43.0	56.5	0.0	555.69	-16.0
145	24.2	187.0	151.3	167.8	48.1	74.4	0.0	652.74	-15.5
144	32.3	187.0	161.5	167.8	51.3	89.3	0.0	689.14	-15.0
143	43.1	202.9	173.2	167.8	57.8	107.1	0.0	751.90	-14.5
142	49.7	218.1	180.3	167.8	60.6	120.0	0.9	797.37	-14.0
141	56.5	218.1	191.3	167.8	65.2	132.9	7.4	839.20	-13.5
140	63.7	218.1	196.0	167.8	70.3	144.8	16.6	877.29	-13.0
139	68.2	218.1	203.0	167.8	76.8	162.6	21.2	917.78	-12.5
138	71.8	218.1	212.4	202.3	83.3	181.5	27.7	997.04	-12.0
137	78.4	234.1	221.9	202.3	87.0	193.4	49.8	1066.70	-11.5
136	82.6	234.1	230.5	202.3	91.6	207.3	66.4	1114.62	-11.0
135	87.1	265.2	244.6	223.4	99.5	228.1	87.6	1235.45	-10.5
134	90.9	265.2	254.0	236.7	104.1	242.0	111.6	1304.56	-10.0
133	94.5	265.2	262.6	236.7	108.3	257.8	131.0	1356.17	-9.5
132	97.8	275.6	268.9	239.1	114.7	267.8	149.4	1413.31	-9.0
131	99.6	288.8	277.5	239.1	119.8	278.7	192.8	1496.23	-8.5
130	101.4	288.8	281.4	239.1	124.0	285.6	212.1	1532.42	-8.0
129	102.9	324.8	291.6	274.4	132.3	288.6	238.9	1653.44	-7.5
128	104.4	326.9	294.8	274.4	138.3	292.5	262.0	1693.20	-7.0
127	105.6	326.9	303.4	296.3	142.0	296.5	281.3	1752.02	-6.5
126	105.9	326.9	310.4	296.3	146.2	300.5	292.4	1778.56	-6.0
125	106.5	340.0	317.5	296.3	152.6	302.5	308.1	1823.51	-5.5
124	106.5	346.9	324.5	299.5	156.4	304.4	317.3	1855.54	-5.0
123	106.5	346.9	328.5	299.5	164.2	304.4	325.6	1875.62	-4.5
122	106.5	355.3	334.7	315.1	167.5	306.4	333.0	1918.48	-4.0
121	106.5	377.4	340.2	344.1	176.3	309.4	340.4	1994.29	-3.5
120	106.5	410.0	343.4	345.7	184.1	312.4	344.1	2046.05	-3.0
119	106.5	410.0	348.8	345.7	191.5	313.4	345.9	2061.77	-2.5
118	106.5	410.0	356.7	346.5	200.3	315.4	347.8	2083.03	-2.0
117	106.5	432.1	360.6	361.4	204.5	316.3	347.8	2129.15	-1.5
116	106.5	432.1	363.7	361.4	211.4	317.3	348.7	2141.13	-1.0
115	106.5	454.3	370.0	361.4	217.9	317.3	349.6	2176.97	-0.5
114	106.5	458.4	373.9	405.3	223.9	321.3	353.3	2242.61	0.0
113	106.5	481.3	378.6	425.7	228.1	323.3	354.2	2297.63	0.5
112	106.5	481.3	381.8	425.7	233.6	324.3	357.9	2310.99	1.0
111	106.5	510.4	386.5	440.6	240.6	325.3	357.9	2367.61	1.5

* (Avg. Max Count = 155.45; Avg. Max Temp = -20.7).

NOTE: Satellite digital counts above defined thresholds (ex. 111) vs. area multiplied with time intervals between observations (km² hr). The "ATI" column represents the sum of each area column multiplied by the time interval for the cluster duration (ATI's corresponding to different digital count thresholds). The last column represents the temperature corresponding to the given digital count (first column).

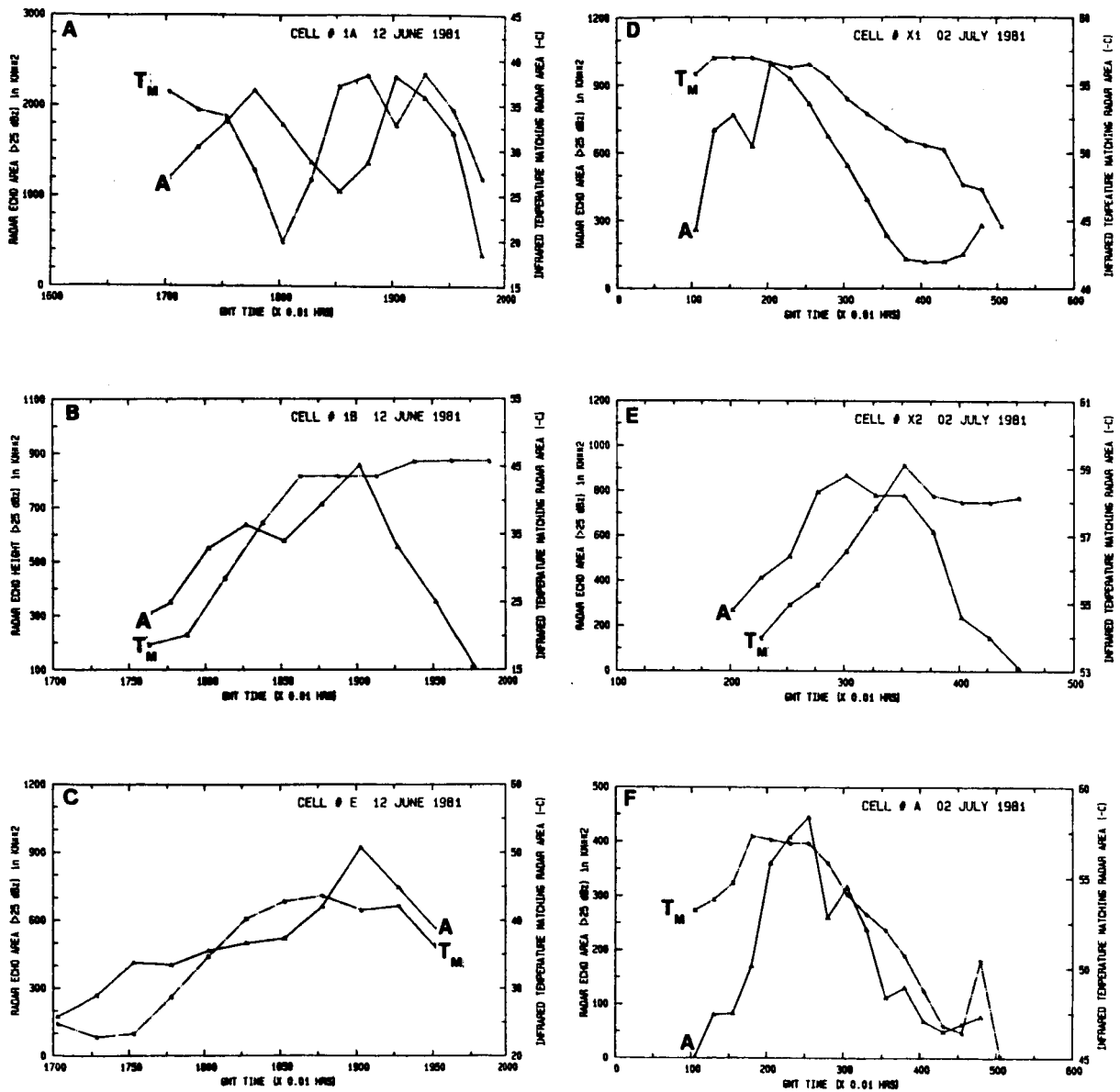


Fig. 4: Trends of radar echo area (A) and infrared temperature matching radar echo area (T_M) for the 18 analyzed clusters.

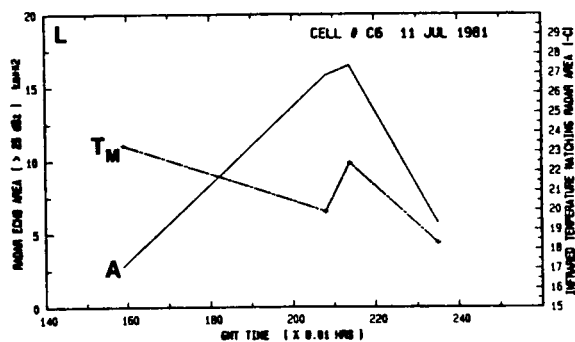
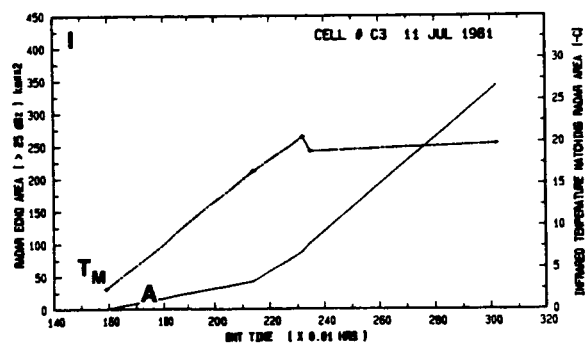
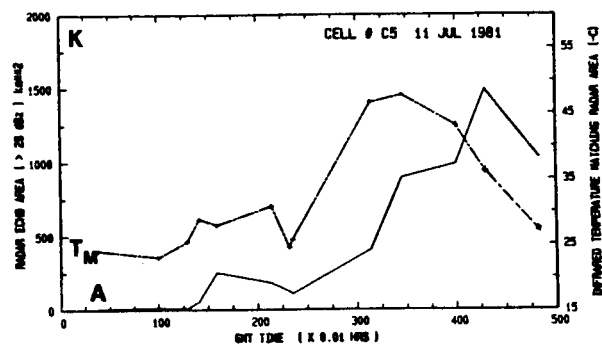
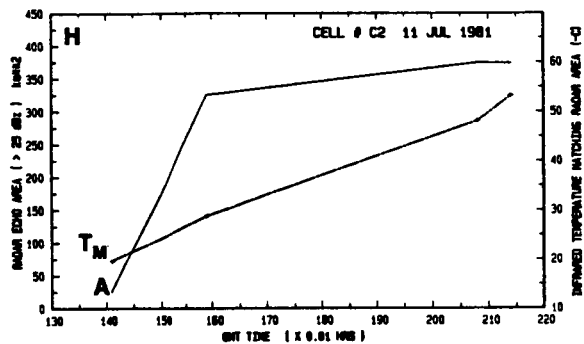
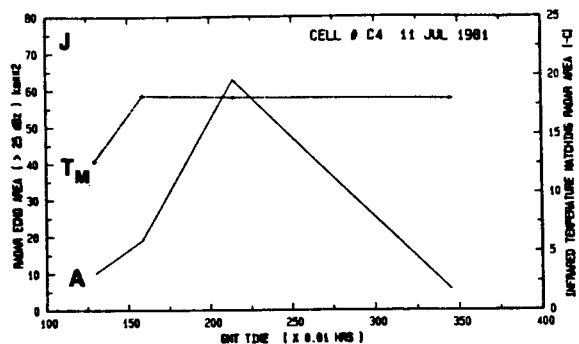
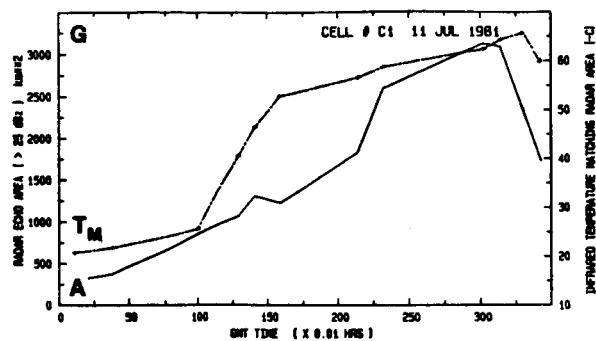


Fig. 4: (continued).

ORIGINAL PAGE IS
OF POOR QUALITY

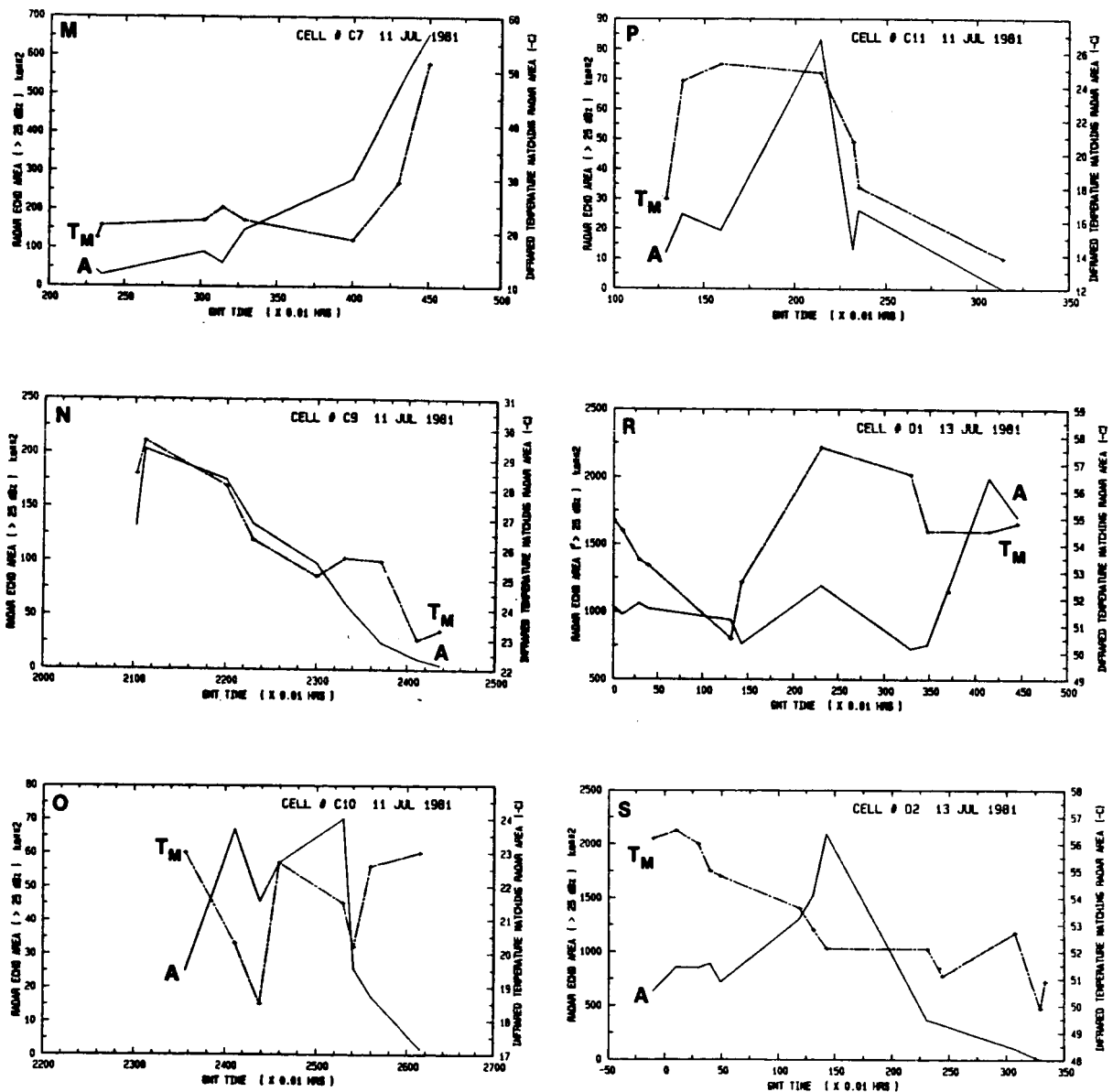


Fig. 4: (continued).

Figure 5A-S displays the maximum radar reflectivity (Z), the temperature of infrared maximum count (T_{MX}), and the maximum echo height (H) for reflectivity values >20 dBz on an interpolated step-by-step basis for all six cells. Again, as in Fig. 4, the similarity of cluster evolution and the time lag between radar and satellite are evident.

A 30-min lag between both the radar maximum echo height, the maximum reflectivity, and the satellite minimum temperature is evident in some of the cells (1A, 1B, E). The effect of cirrus debris is visible in Fig. 5B (Cell 1B), but not in Fig. 5E (Cell X2), as noted in Fig. 4E; the cause might be that T_M (in Fig. 4) is a temperature threshold matching the radar ATI, while T_{MX} (in Fig. 5) is the temperature of the IR maximum count for the whole cell duration. The cirrus debris effect is also visible in Fig. 5J and O.

As mentioned earlier, four convectively active days were under consideration: June 12, July 2, July 11, and July 13. Consecutive time steps with both radar returns and satellite visible and IR images were constructed for the four mentioned days. A total of 67 images in IR, 13 images in visible, and 67 radar PPI figures were produced. The satellite sector of interest adjusted to avoid cloud features suspected of not being detected by the radar is contoured in the infrared images (black continuous line). The infrared contours represent 4°C temperature steps, with the first contour representing a given fixed temperature. No wind adjustment was applied to the satellite images.

Thirteen consecutive time steps with both radar returns and satellite visible and infrared images for the 12 June clusters are displayed in Fig. 6A (Doneaud *et al.*, 1984c). Satellite times were chosen to be as close to the radar times as possible. The times are marked in the figure. The event lasted three hours. The three clusters (1A, 1B, and 1E) under consideration are individualized in the radar PPI images (dashed lines). In fact, Cell E represents a part of cluster 1A which developed independently. The growth and decay periods of the clusters are evident in all three sequences of images. There are differences between radar, visible, and infrared features which are explicable. It appears that the visible cloud image is closer than the IR image to the radar return features, as evidenced in Fig. 6A at 1732 GMT. Two lines of radar echoes oriented southwest to northeast are apparent in the radar PPI. These lines are discernible in the visible image but not in the infrared image. Similar situations could be mentioned at 1738 GMT (1746 GMT radar time) and at 1759 GMT (1801 GMT radar time). The cirrus spissatus were excluded from the computation at 1759 GMT, as they appear to be detached horizontally from the radar echo cluster. The embedded convective clouds are no longer visible in the radar PPI at 1759 GMT; the definition of the area of interest for the cluster 1A was shifted southward to a dramatically smaller area between 1738 and 1759 GMT. This demonstrates how radar data were used to adjust the satellite sector of interest to exclude non-precipitating clouds (i.e., cirrus debris).

ORIGINAL PAGE IS
OF POOR QUALITY

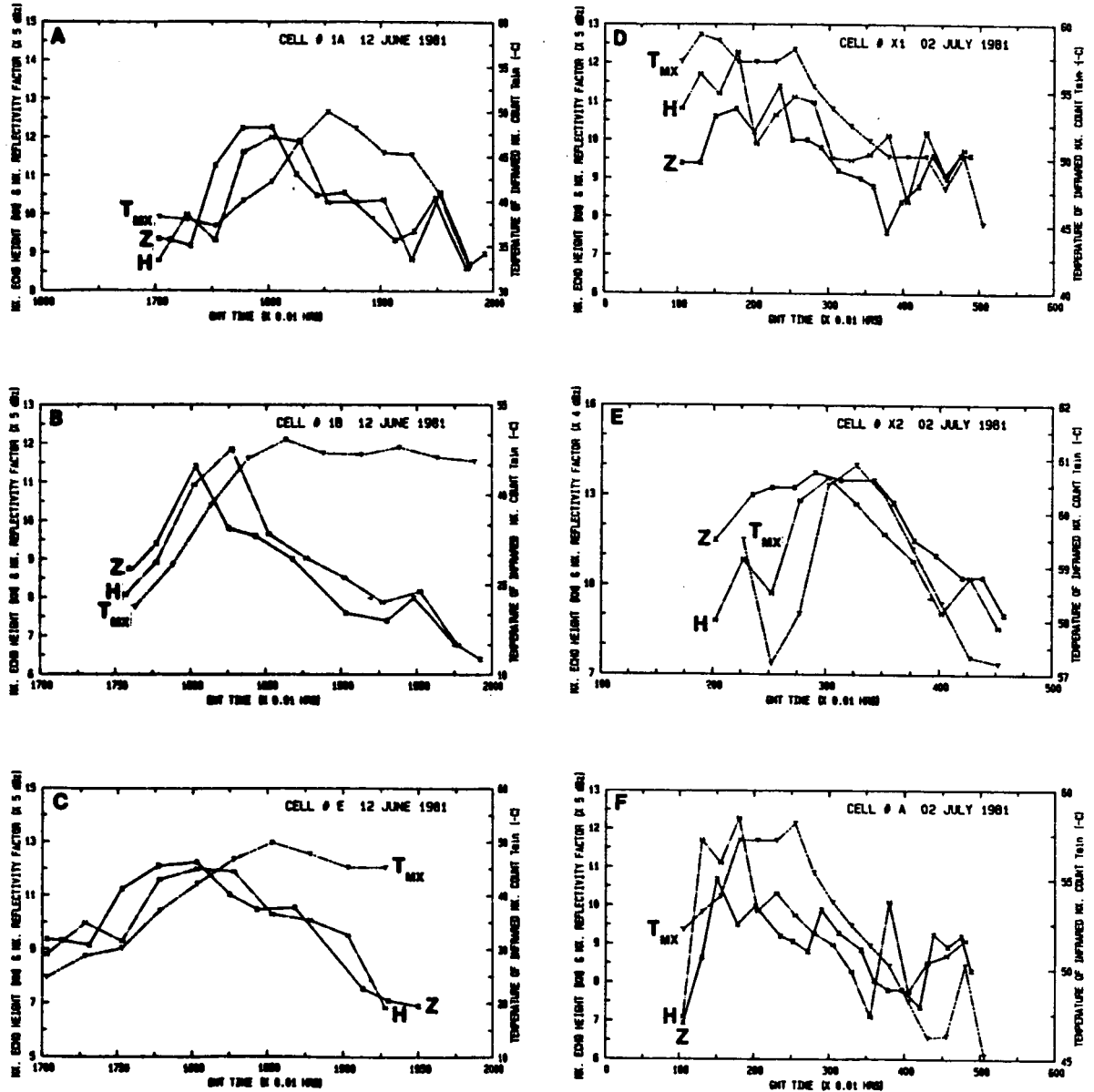


Fig. 5: Trends of radar maximum echo height (H), maximum reflectivity (Z), and temperature of infrared maximum count (T_{MX}) for the 18 analyzed clusters.

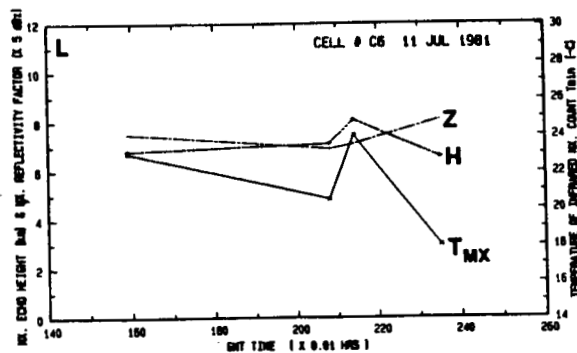
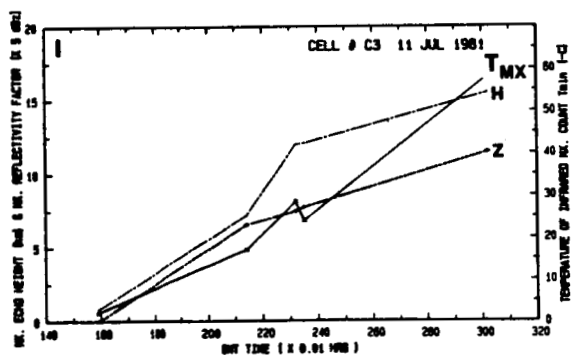
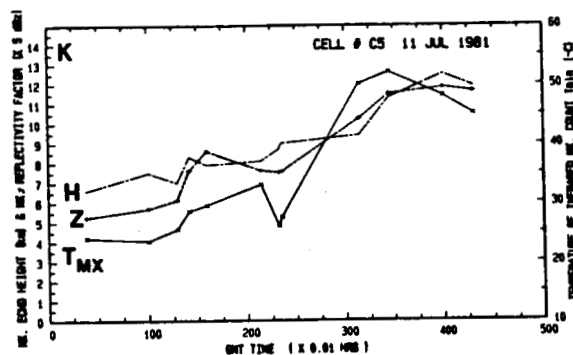
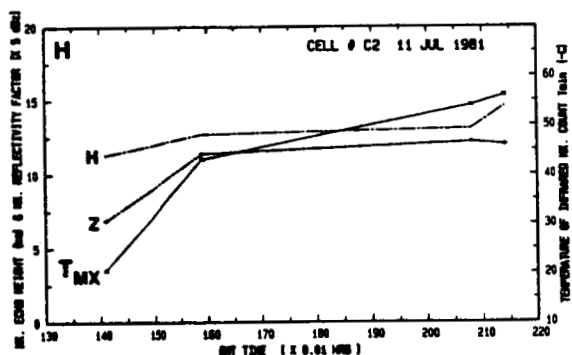
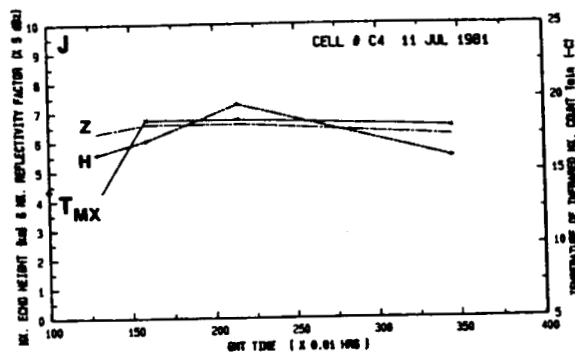
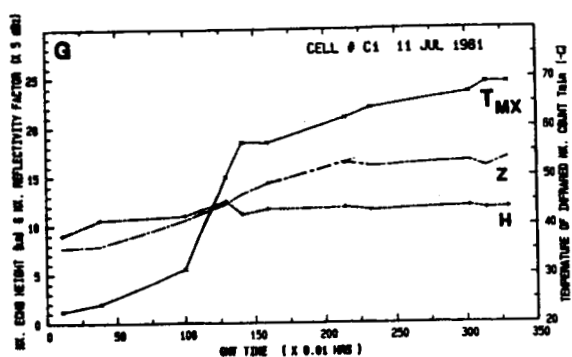


Fig. 5: (continued).

ORIGINAL PAGE IS
OF POOR QUALITY

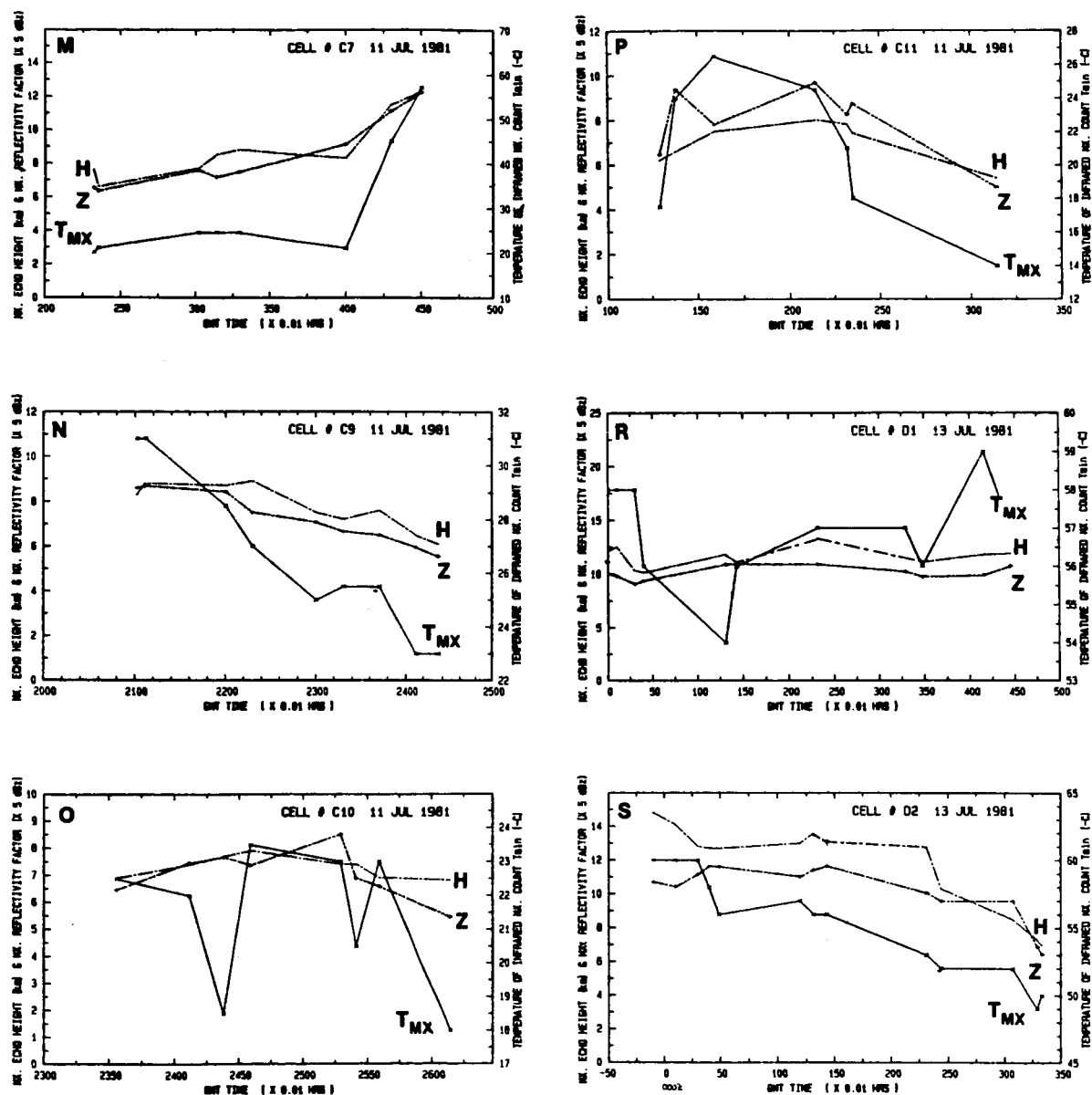


Fig. 5: (continued).

A visual inspection of the images (Fig. 6A) emphasizes the multicellular structure of the cluster. Four cells are visible in the first radar and infrared images (1657 GMT and 1702 GMT, respectively.) The northerly located cells emerged and decreased in brightness and radar reflectivities, vanishing after 1827 GMT. Only cirrus debris is still visible in the IR images along the northern border of the PPI after 1827 GMT. Concomitantly, the southerly located cell (E) was behaving independently. It grew until 1841 GMT as a convective event, then decayed and disappeared after 1929 GMT; at that time, cirrus debris was still visible in the satellite image, but was out of the radar effective range to the northeast. Cell 1B grew until 1815 GMT, then decayed and vanished by 1955 GMT. So, as inferred by the image sequences, the cluster 1A increased and decreased twice before vanishing, while the cluster 1B pulsed only once. These multicellular clusters do not alter the radar ATI product, as the ATI is the echo area integrated over the duration of the cell.

The step-by-step radar reflectivities for >25 dBz exhibited by contours with a 10-dBz interval for the 2 July 1981 clusters and corresponding satellite IR features are presented in Fig. 6B. The radar sectors used to delineate the echo clusters are displayed on each radar PPI image; the satellite subjective sectors are displayed on the satellite images. The IR contours represent 4°C temperature steps as in Fig. 6A. The multicellular structure of Cluster X1 is evident. Cluster X2 starts as a single cell and develops into a multicellular structure as it matures. In the satellite images as well as in the radar PPI, Cell X1 grows until 0128 GMT (two consecutive time steps); it slowly decays until 0241 GMT, and more rapidly until the end at 0503 GMT. Cell A is a part of Cluster X1, which grew until 0241 GMT, then slowly decayed during the next two consecutive time steps. The evolution of Cell X2 as followed by radar data suggests that its development (in the outflow region of a previous cluster) is well extended horizontally and vertically, and is part of a southwest-northeast oriented echoline with a cellular structure. The maximum vertical extension of all clusters occurs during the first half of their lifetime.

Twenty-four consecutive time steps with both radar returns and satellite infrared images (over a period of ~8 hours) for the 11 July 1981 clusters are displayed in Fig. 6C. The times are marked in the figure. The growth and decay periods of the clusters are evident in both sequences of images. There are differences between radar and infrared features which are explicable; however, the main clusters are present on both sequences of images. Ten clusters were selected from the numerous clusters developed over the radar PPI; lines of cells (C9), cells (C11), clusters (C10), and supercell (C1) were considered in the analysis. Moving east, the C1 supercell merged into the mesoscale convective complex (Fankhauser *et al.*, 1983; Doneaud *et al.*, 1981b). Cluster C9 and cluster C10 have similar tracks. The clusters were recorded first on the southwest corner of the radar PPI and then moved northeast, with their maximum stage of development closer to the radar location; afterwards, they vanished on the

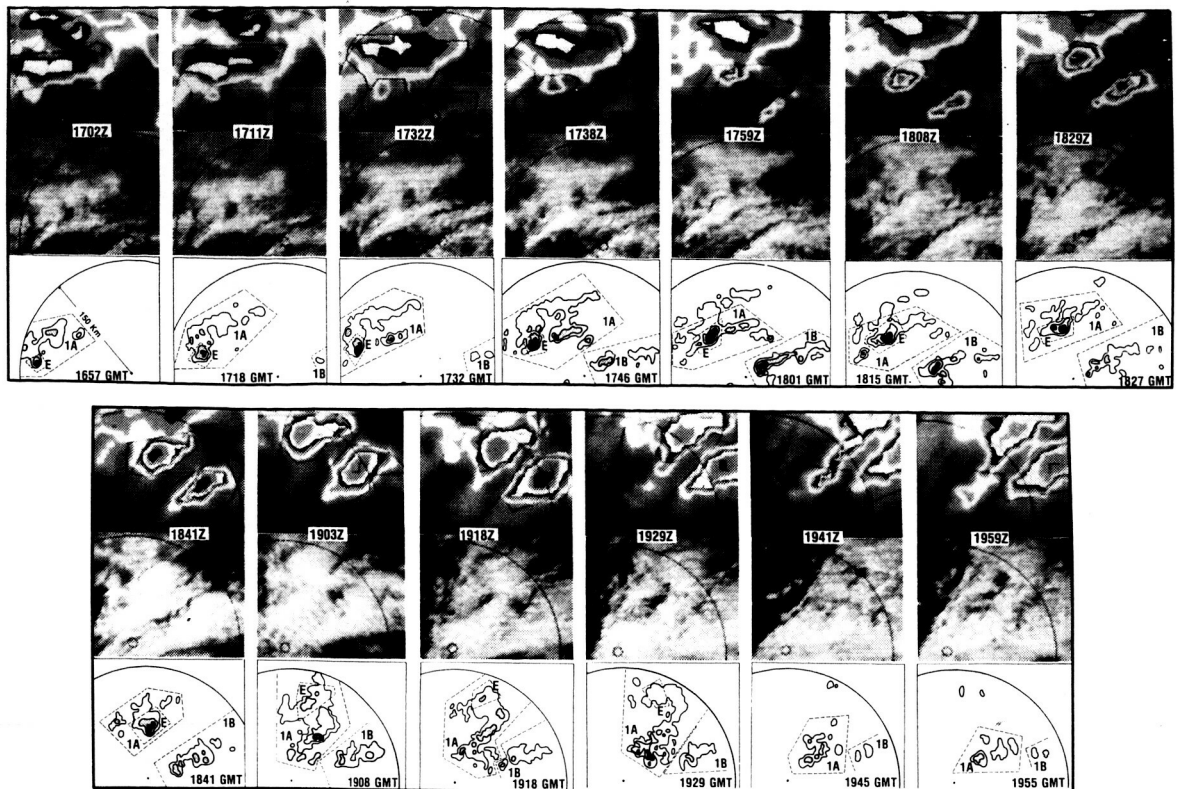
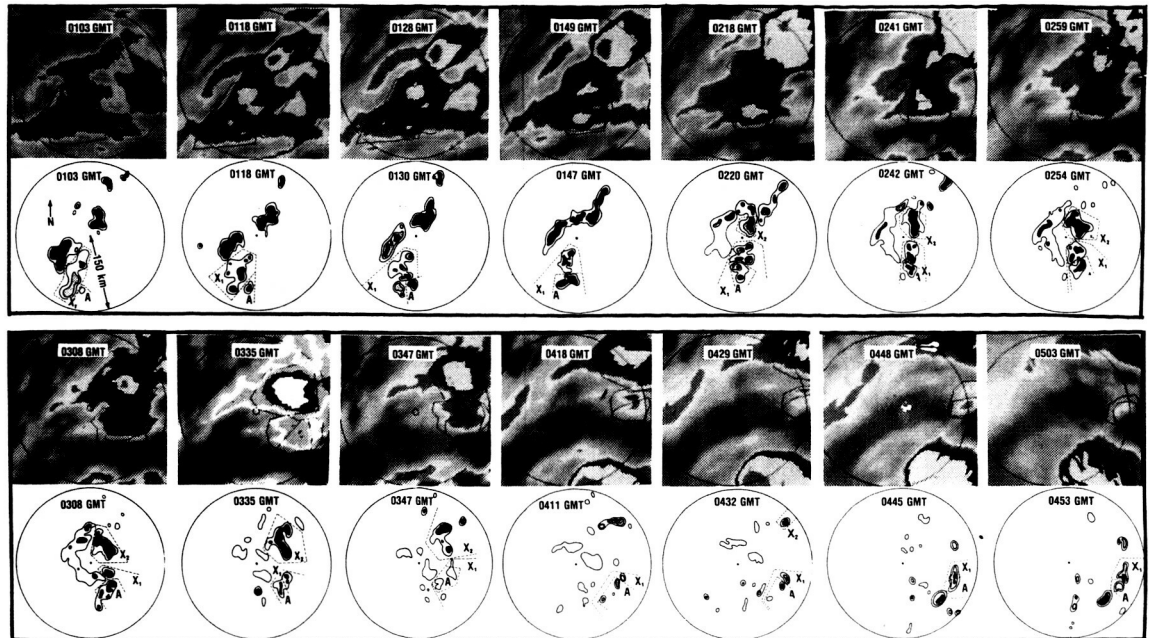


Fig. 6: Sequences of GOES Rapid Scan Satellite Pictures (IR and VIS) and radar reflectivity patterns for the 12 June, 2, 11, and 13 July clusters. Continuous contours on infrared images represent the satellite sectors of interest, while the dashed contours on radar PPI represent the radar sector of interest.

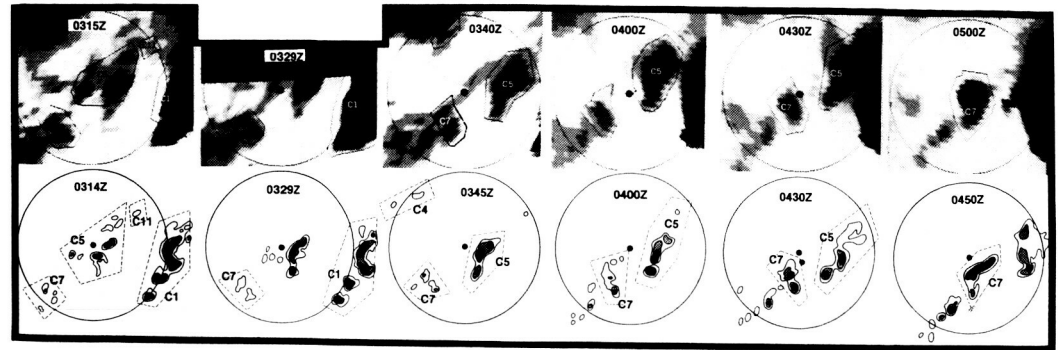
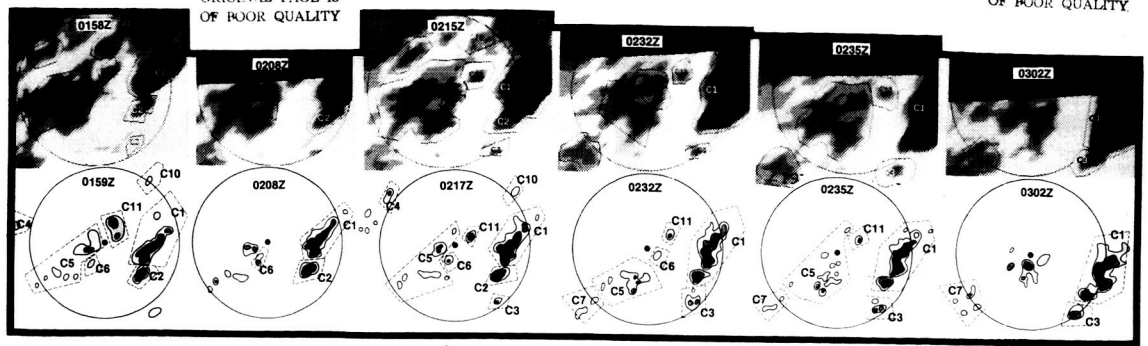


FOLDOUT FRAME

FIGURE 6 (continued)

ORIGINAL PAGE IS
OF POOR QUALITY

ORIGINAL PAGE IS
OF POOR QUALITY



1 FOLDOUT FRAME

FIGURE 6 (continued)

2 FOLDOUT FRAME

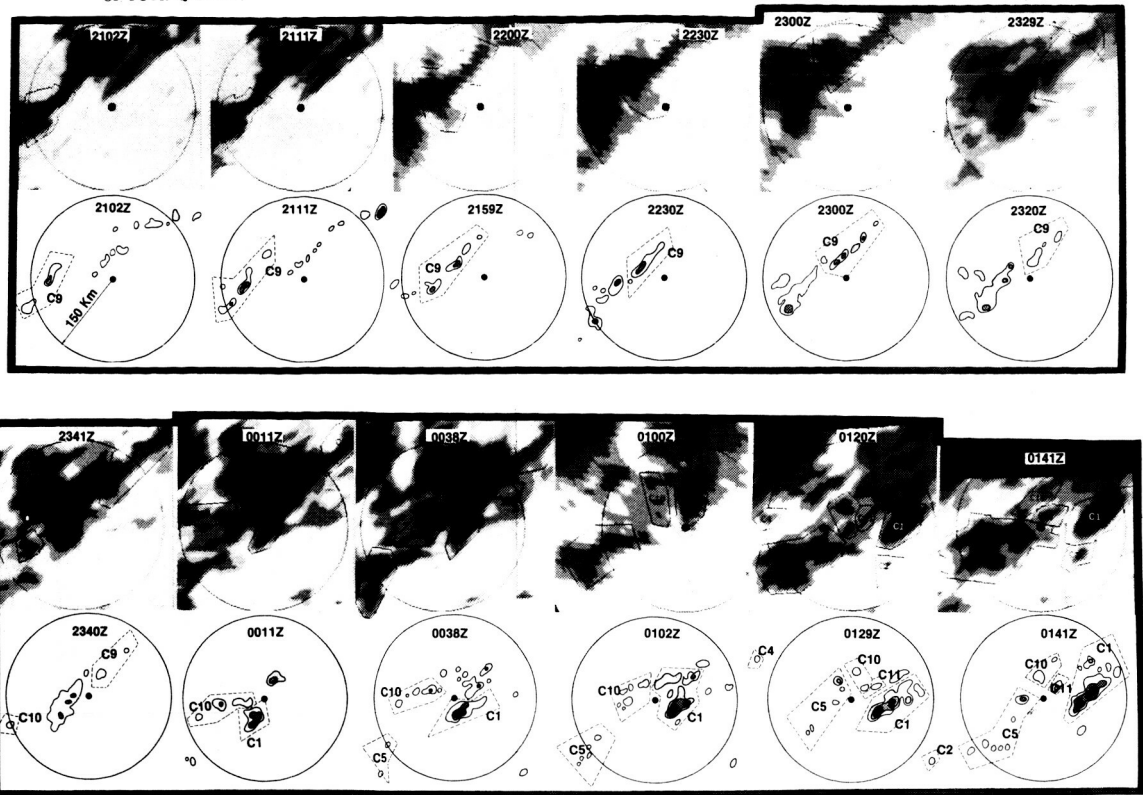


FIGURE 6 (continued)

FOLDOUT FRAME

FOLDOUT FRAME

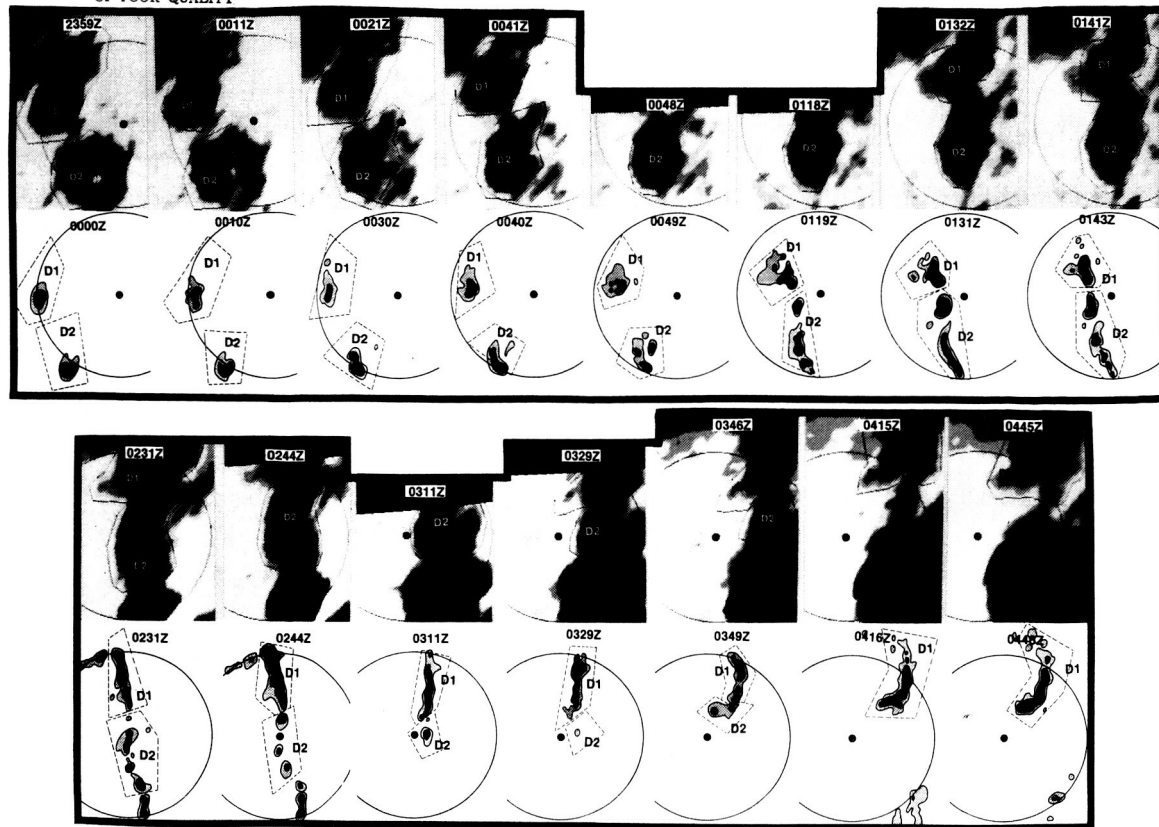


FIGURE 6 (continued)

(THIS PAGE INTENTIONALLY LEFT BLANK)

northeast corner of the PPI. The supercell C1 was first recorded south of the radar location, and then developed dramatically, moving east. Later, Cell C5 merged with supercell C1 (satellite pictures, 0430Z) and became a mesoscale convective complex. Finally, Cell C7 also merged (after 0500Z) with the mesoscale convective complex. The 10 clusters selected are clearly visible in both PPI and IR images.

The step-by-step radar reflectivities for >25 dBz exhibited by contours with a 10-dBz interval for the 13 July 1981 clusters and corresponding satellite IR features are presented in Fig. 6D. As in Fig. (6A,B,C), the radar sectors used to delineate the echo clusters are displayed on each radar PPI image, while the satellite subjective sectors are displayed on the satellite images. Two clusters were selected, D1 and D2, and displayed on 15 images, over a period of ~5 hours. D1 was first recorded on the west border of the radar (150 km) range, and D2, south of D1. Both cells became lines of cells and moved eastward, having similar speed. D2 started to decay at 0231Z and vanished at 0349Z. D1 continued to grow and to move eastward until 0448Z, the last radar recording time.

3.2 Cluster Lifetime Analysis

A summary of radar and satellite products for the 18 analyzed clusters is presented in Table 3A-B.

Columns (2) to (5) represent radar products, columns (7) to (11) represent independent satellite products, while columns (12-14) represent satellite products obtained as a combined radar versus satellite analysis. The digital count thresholds matching radar ATI's and the respective minimum temperatures, as well as the satellite ATI (columns 12-14), were computed for the storm lifetime using histograms. The histograms are presented for the 18 clusters considered in Fig. 7A-S. The dashed-dotted line represents the satellite determined ATI (on a step-by-step basis) and its respective digital count. These histograms were computed using cloud areas multiplied by the time and summed over the duration of the storm (ATI) for the abscissa; the ordinate is the maximum digital count over the storm's lifetime. These histograms differ from those presented in Sec. 3.1 not summed over the cell duration.

A visual inspection of both radar and satellite products (in Table 3A) emphasizes variable geometries (physical appearance) of the 18 considered clusters. For instance, as viewed by satellite, the 2 July clusters are higher (X1, X2, A) than the 12 June clusters. The satellite products (columns 7-13) are always greater for 2 July than 12 June. The MEH (column 3) average is only slightly higher (0.96 km) for 2 July. The cluster with the largest MEH (X2, MEH = 14.4 km) did not generate the greatest amount of rain.

The 18 clusters (Table 3A-B) exhibit a large spectrum of ATI values ranging from 7.3 km² hr for cluster C6 to 7, 247.1 km² hr for cluster D1. The rain volume varies from 19 km² mm (C6) to

TABLE 3A
Characteristic Products of Bowman Radar and GOES Satellite Data for Six Clusters (or Cells) of Summer 1981

RADAR DATA					SATELLITE DATA											
Cell Date	Cell No. and Duration (hrs)	Max dBz	Max Echo Height (km)	ATI (km ² hr)	Rain Vol (km ³ mm)	λ	Maximum Digital Count	Temp of IR T _{MX} (-°C)	Average* of IR Max Count	Average* Temp of IR T _{MX} (-°C)	Averaged* Vis Max Count	Digital Count Thresh Matching Radar ATI	Temp Matching Radar ATI T _{MA} (-°C)	ATI (Satellite) (km ² hr)		
(0)	(1)	(2)	(3)	(4)	(5)	(6)	(7)	(8)	(9)	(10)	(11)	(12)	(13)	(14)		
06/12	1A 2.96	61	12.2	4,625	16,119	IR VIS	195 66	50.2	186.5	41.5	62.8	178.70 57.73	33.0	4,534 4,534		
06/12	1B 2.50	57	12.1	1,117	4,082	IR VIS	194 65	49.2	190.1	45.1	63.0	189.09 59.36	45.0	1,169 1,169		
06/12	E 2.55	61	12.2	1,302	6,831	IR VIS	195 64	50.2	188.6	43.6	61.0	185.68 57.85	41.0	1,221 1,221		
07/02	X1 3.83	57	12.5	1,897	11,001	IR	204	59.2	198.5	53.5		201.21	56.4	1,876		
07/02	X2 2.55	55	14.4	1,338	1,027	IR	207	61.2	203.6	58.6		202.47	58.0	1,243		
07/02	A 3.83	53	12.5	704	4,268	IR	204	59.2	198.8	53.8		201.39	56.5	722		

*Averaged over the cell lifetime.

TABLE 38

Characteristic Products of Miles City Radar and GOES Satellite Data for Twelve Clusters (or Cells) of Summer 1981

Cell Date	RADAR DATA				SATELLITE DATA									
	Cell No. and Duration (hrs)	Max dBZ	Max Echo Height (km)	ATI (km ² hr)	Rain Vol (km ³ mm)	λ	Maximum Digital		Temp of IR		Average* Temp of IR		Digital Count Thresh	
							Count	Count	Max Count	Max Count	Average* Max Count	Average* Max Count	Count	Count
(0)	(1)	(2)	(3)	(4)	(5)	(6)	(7)	(8)	(9)	(10)	(11)	(12)	(13)	(14)
07/11	C1 3.32	63.6	18.0	5,361.4	43,771	IR	214	-69.0	195.6	-50.6		205.6	-60.6	5,417.9
07/11	C2 0.65	61.0	14.6	145	1,599	IR	201	-56.0	178.5	-33.5		188.0	-43.0	146.0
07/11	C3 1.22	59.0	15.5	170.1	1,645	IR	203	-58.0	167.5	-26.8		179.9	-37.9	171.1
07/11	C4 2.32	37.2	7.0	137	1,289	IR	151	-18.5	148.0	-17.0		150.9	-18.4	127.3
07/11	C5 4.21	61.1	14.4	2,236.2	12,477	IR	197	-52.0	176.7	-31.7		184.6	-39.6	2,237.3
07/11	C6 0.60	41.9	8.1	7.3	19	IR	162	-24.0	157.0	-21.5		157.9	-21.9	7.4
07/11	C7 2.30	61.2	12.5	607.2	3,550	IR	202	-57.0	168.4	-27.2		184.1	-39.1	608.8
07/11	C9 3.36	43.4	9.0	397.1	1,101	IR	176	-31.0	167.1	-26.6		169.6	-27.8	419.0
07/11	C10 2.42	47.4	8.6	129.1	340	IR	161	-23.5	156.7	-21.3		157.0	-21.5	125.5
07/11	C11 1.77	45.9	8.4	47.2	181	IR	167	-26.5	155.6	-20.8		162.2	-24.1	47.7
07/13	D1 5.75	60.3	13.3	7,247.1	38,446	IR	207	-62.0	202.4	-57.4		198.5	-53.5	7,257.6
07/13	D2 4.47	58.5	15.5	3,469.9	17,649	IR	205	60.0	200.5	55.5		198.6	53.6	3,415.3

*Averaged over the cell lifetime.

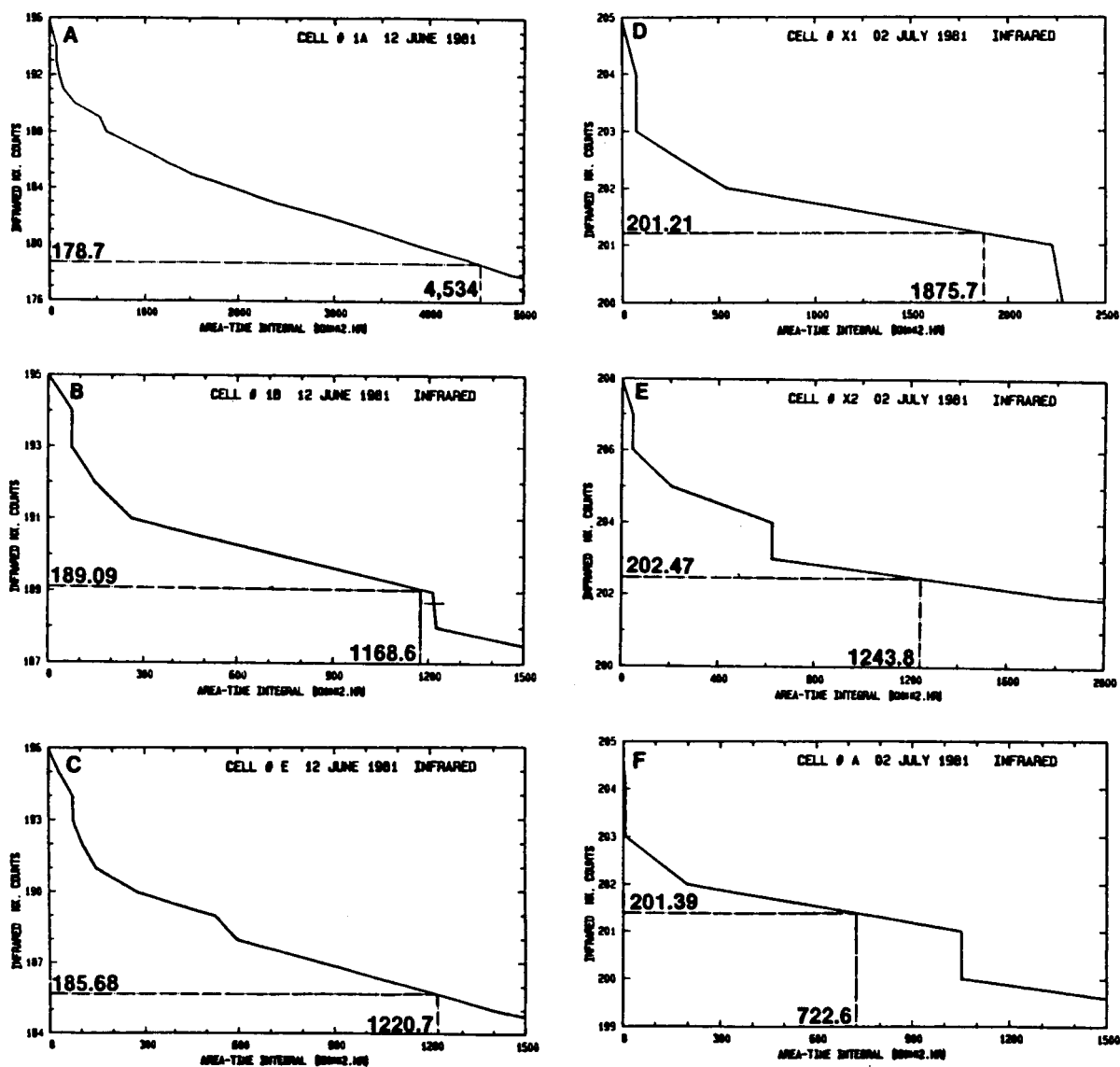


Fig. 7: Histograms of VIS (A) and IR (B) digital counts vs. satellite ATI's for the 18 cells; the radar ATI and the correspondent digital count are also indicated.

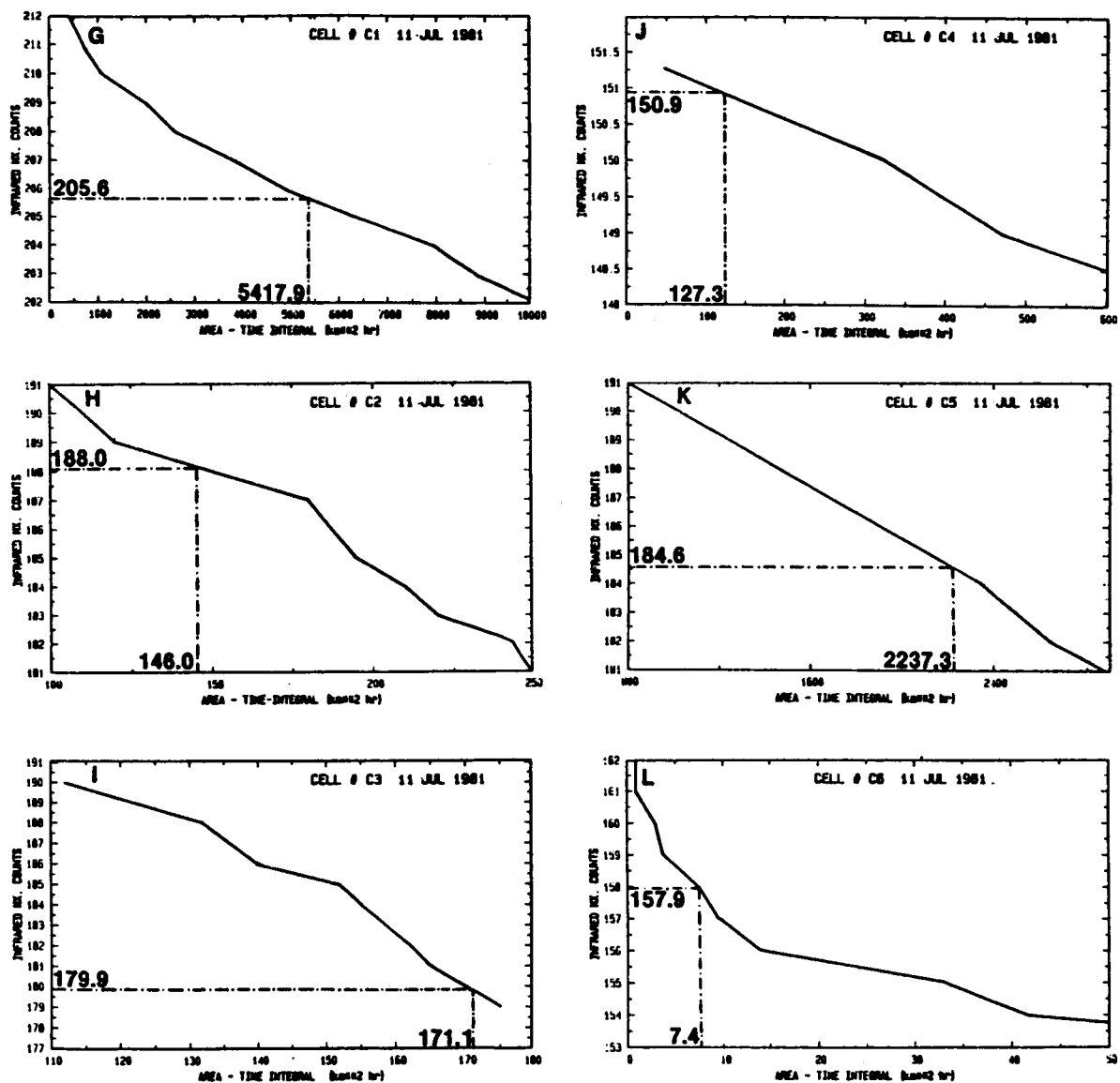


Fig. 7: (continued).

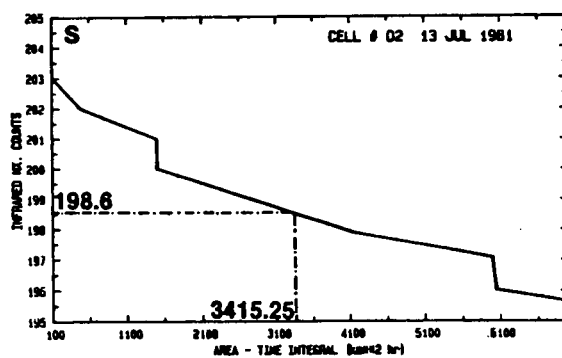
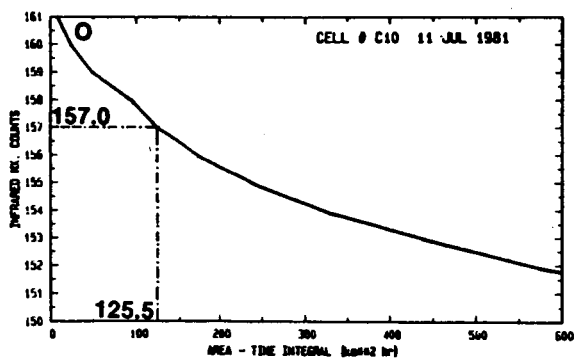
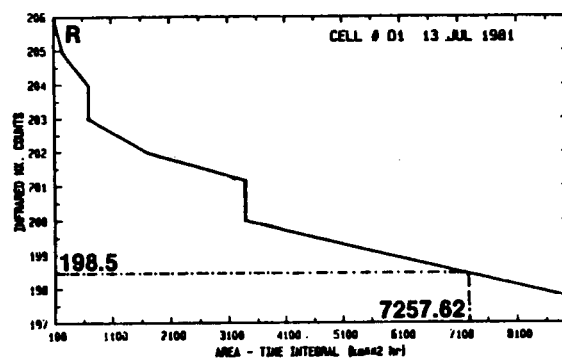
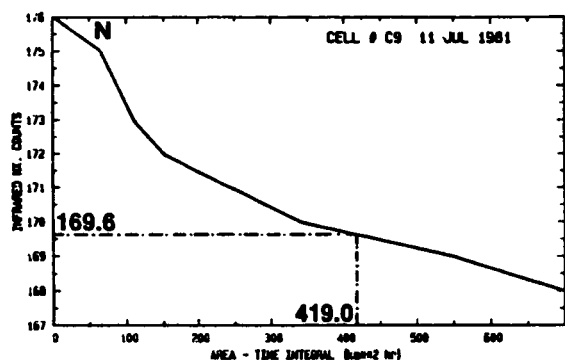
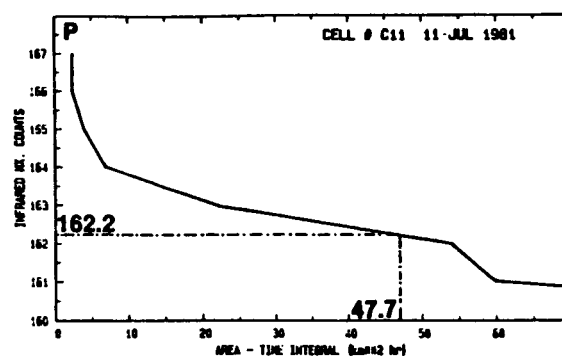
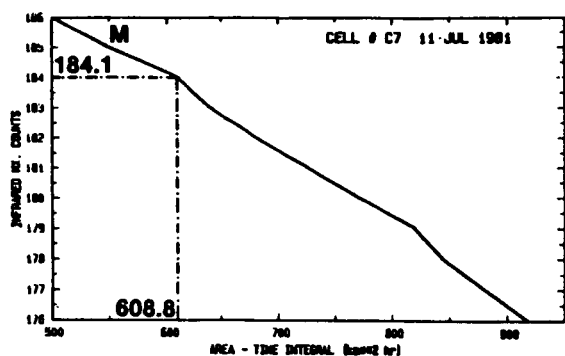


Fig. 7: (continued).

38,445.6 km² mm (D1); a large diversity in cluster size is demonstrated by this data set. The absolute temperature of the IR maximum count averaged over the cell lifetime is always smaller than the absolute value of the minimum temperature (the maximum digital count) for the cluster lifetime (Table 3A-B).

The main purpose of this investigation is to compute convective rain volume over a moving targeted area by application of the ATI technique based only on satellite data. As such, the key element is to determine ATI from independent satellite data without the additional constraint of radar data. This is possible if trends of satellite products (Table 3A-B, columns 7, 8, 9, and 10) generated independently are similar to those of satellite products based upon radar observations as done here. An independent satellite quantity which defines the most appropriate digital count that matches the radar ATI for a given cluster would be a solution. For instance, regression curves correlating satellite digital count thresholds to satellite IR maximum count values (Fig. 8), or to satellite IR maximum count values averaged over the duration of the cell (Fig. 9), had to be identified. The mentioned quantity (the satellite IR maximum count averaged over the cluster duration) could also be related to weather conditions if the vertical structure of the air mass is taken into consideration (Doneaud et al., 1987).

For the 18 clusters considered in this investigation, the linear regression relating the IR maximum count values averaged over the duration of the cluster to the IR temperature, which matches the radar ATI (Fig. 9), generated a high correlation coefficient of .93, a standard error of estimate of 13.3, and a range of the IR temperature matching the radar ATI of -33% to +67%.

A regression analysis with an acceptable correlation coefficient gives more accurate estimates of delineated rain areas than a single or multiple thresholds. The next step is to convert the IR temperature matching the radar ATI (Fig. 9) to digital counts; the digital counts are related to satellite ATI by a histogram for that particular cluster, as presented in Fig. 7A-S for the 18 clusters analyzed. The total rain volume is finally obtained by applying an ATI versus rain volume relationship (see Fig. 10) determined for that particular region using radar data (Doneaud et al., 1984a). In other words, rain volume from satellite data is obtained by using two regression lines: one determines the rainy portion of the cloud area (Fig. 9 and the histogram), and the second (Fig. 10), the rain volume from the ATI.

A similar correlation analysis has been worked out by using a linear regression relating the minimum IR temperature (instead of the minimum IR temperature averaged over the cluster lifetime) to the minimum temperature matching the ATI. The scatter of the data as noted in Fig. 8 is less satisfactory.

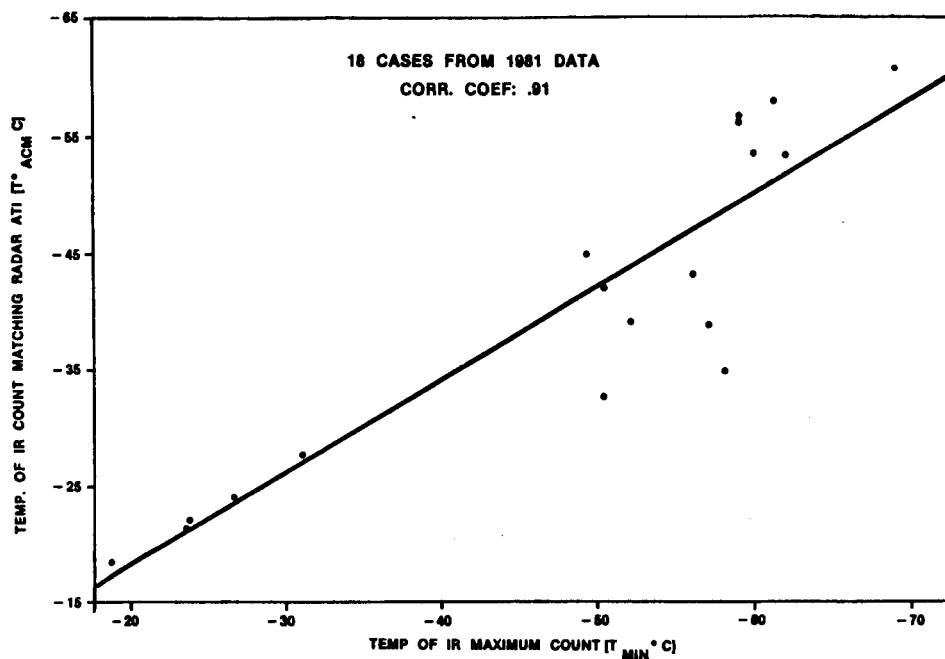


Fig. 8: Scatter and linear regression of temperatures matching radar ATI and IR minimum temperature.

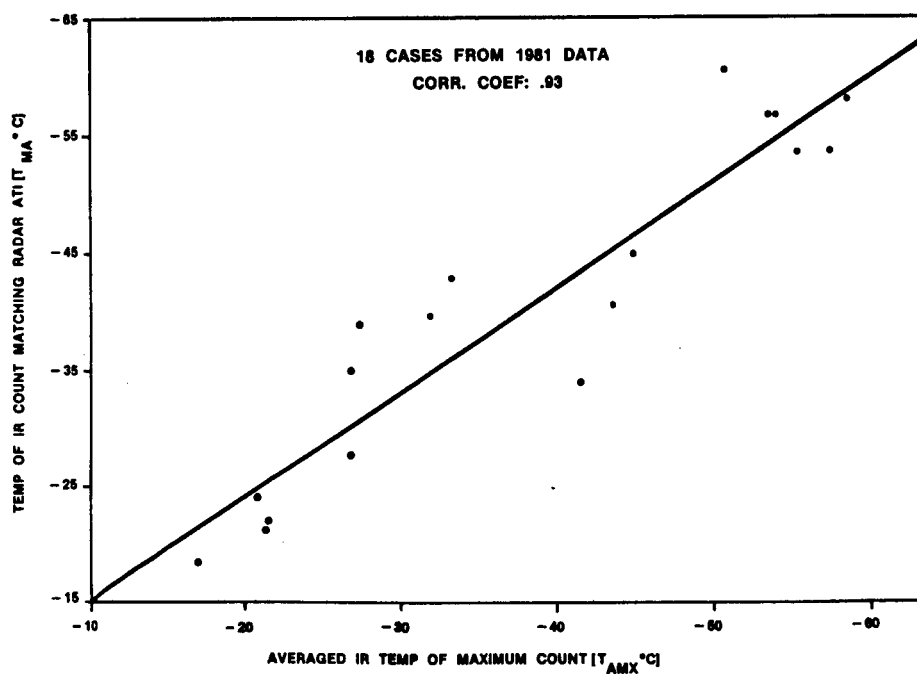


Fig. 9: Scatter and linear regression of temperatures matching radar ATI and average (over the cell duration) temperatures of IR maximum count. Every star represents a cluster.

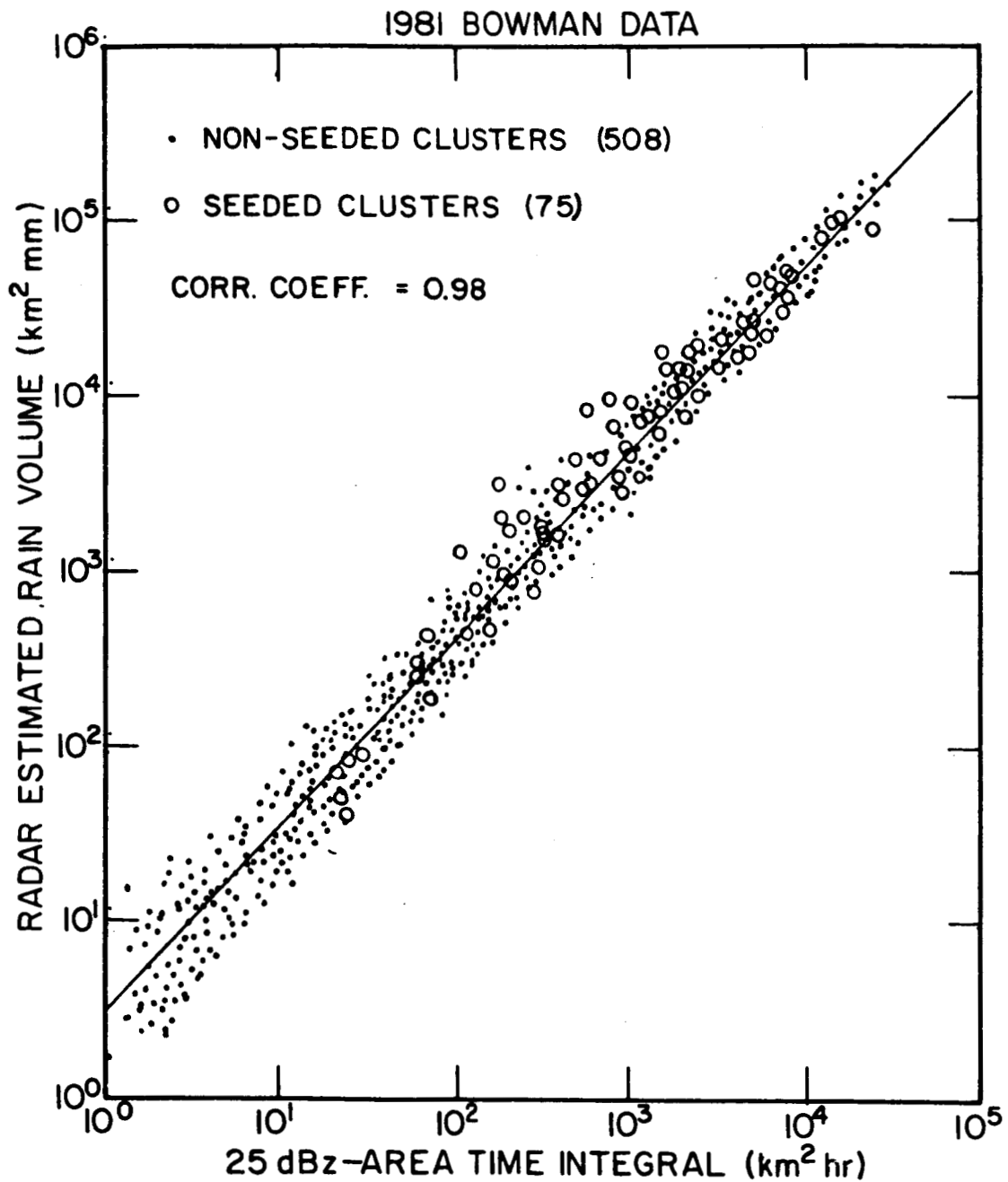


Fig. 10: Scatter and linear regression of total rain volume vs. ATI.

The ATI technique generates only total rain volume estimates of convective cloud systems. Rain rates must be obtained independently of the ATI technique.

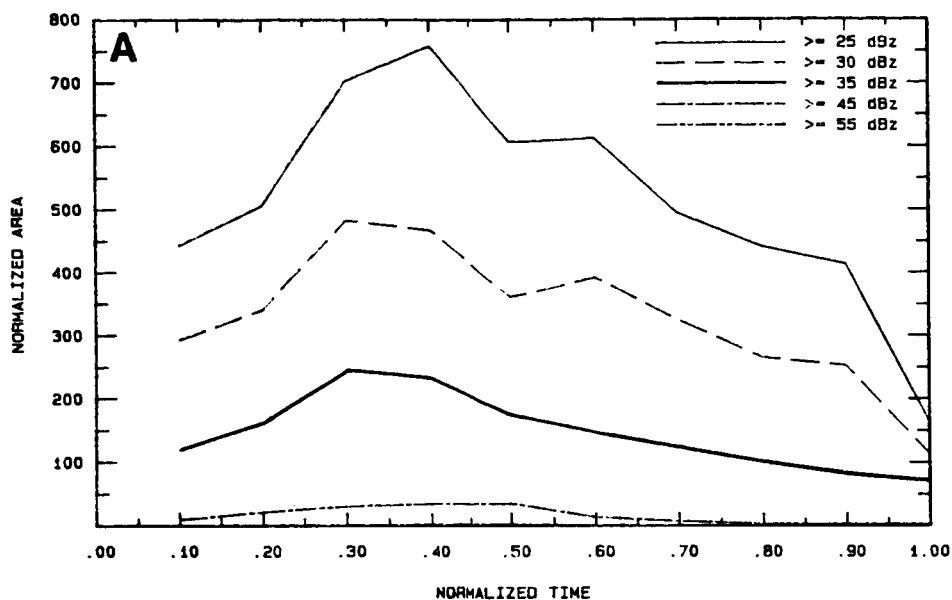
The ATI technique and the procedures followed to apply the technique to satellite data are original. However, a parallel with the two-step technique generally can be used to compute rain volume from satellite data. One step relates cloud area with echo-rain area and the second derives rain volume from the delineated rain area. Griffith *et al.* (1976, 1978, 1981), Woodley *et al.* (1980), Augustine *et al.* (1981), and others, determined brightness (VIS) and minimum temperature (IR) thresholds; while Lovejoy and Austin (1979), Tsonis and Isaac (1985), Rongzhang *et al.* (1985), and others, worked out statistical two-dimensional pattern recognition techniques to delineate the rainy part of the clouds. Segments of cloud histories were used to apportion the total rain volume; and isohyetal maps of rainfall were generated. Rain area and rain volume linear relationships were generally used to derive rain volumes from the delineated areas. The coefficient relating area to volume is an average rain rate and was considered dependent to the echo growth trend.

To delineate the rainy part of a cloud, as mentioned earlier, we propose to use a regression analysis. The regression relates a satellite independent product to a satellite product dependent on radar. The minimum temperature of the maximum IR digital count averaged over the duration of the storm and the ATI were respectively considered in this investigation. For a given storm, the independent satellite product is first computed; then the regression analysis gives the delineated rain area. Finally, the rain volume is obtained by using the delineated area and the ATI versus rain volume relationships. The key element which makes the ATI technique (when applied to satellite data) simple is that it operates on a storm duration basis; variables used are always integrated over the storm lifetime. Previous techniques operated on a time-step basis. By applying the ATI/rain volume relationship to satellite data, errors generated by the complicated multiple area-volume transformation relations are reduced. Similar errors were reduced when the technique was applied to radar data (Doneaud *et al.*, 1984a,b).

The high correlation between the IR maximum count averaged over the duration of the cluster and the IR maximum count which matches the radar ATI is also pointed out by the fact that descriptive models representing the structure of the radar reflectivities and the minimum temperature of infrared digital counts as a function of surface area and time have a similar appearance above a given satellite threshold (Fig. 11A-B). This correspondence is emphasized by the -50°C and the 35-dBz curves highlighted in Fig. 11(A-B). These models were computed by normalizing the six analyzed cluster products and presenting them against normalized time. For warmer thresholds, the multicell structure of the clusters generates multimode digital count trends that appear to be more evident in the satellite products. For individual cases, similar correspondence was found for the aforementioned thresholds.

ORIGINAL PAGE IS
OF POOR QUALITY

RADAR REFLECTIVITY STRUCTURE



SATELLITE DIGITAL COUNT STRUCTURE

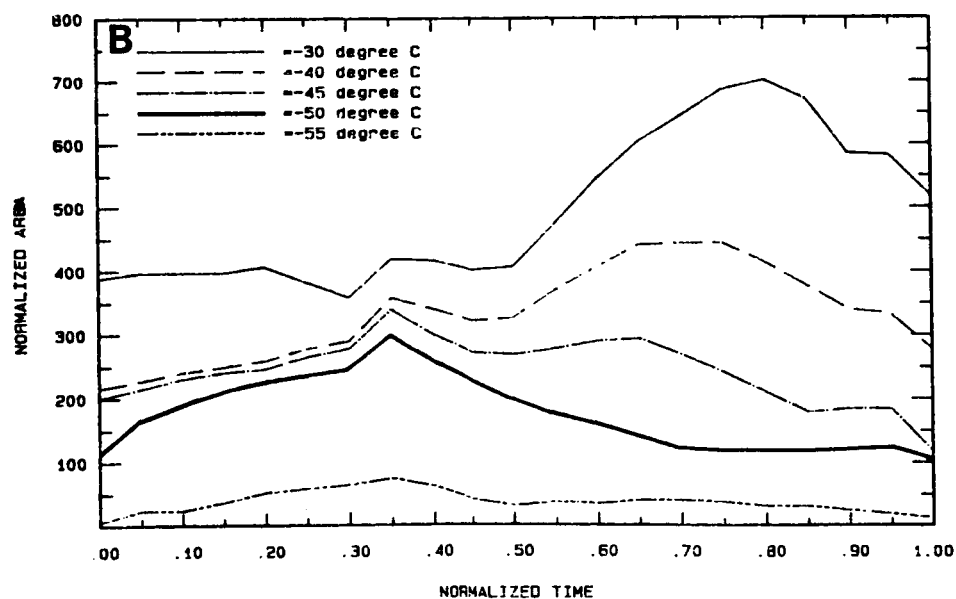


Fig. 11: Structures of radar reflectivities (A), and minimum temperature of IR digital counts (B), as functions of normalized area and time.

4. RESULTS

As mentioned in the previous section, rain volume from satellite data is obtained by using two regression lines (and a histogram), one to determine the rainy portion of the cloud area and the second to get the rain volume. The histogram converts the minimum temperature of the matching ATI to ATI ($\text{km}^2 \text{ hr}$).

The procedure was applied to the 18 cases reported herein. The results are presented in Table 4, column (3). Rain volumes as determined by the conversion of the radar ATI to rain volume are presented in column (2). Using these values for comparison, a standard error was calculated by dividing the difference by column (2), true value. The computed standard error is 0.74 with a standard deviation of ± 0.40 which demonstrates a very reasonable estimation. The "radar ATI" computed rain volume was considered as the true set of estimates (column 2).

The comparison for cluster 1A shows a large difference in rain volumes by the two methods. Further analysis revealed that, in this case, the satellite sectors of interest were greatly limited in an attempt to minimize the influence of cirrus debris. The results would indicate that a portion of the raining cloud was eliminated with the cirrus debris. The method shows promise and indicates that greater care in storm definition will be necessary.

To simplify the procedure, a regression between satellite ATI and average IR minimum temperature was established. Figure 12 presents the regression for all 18 cases with a correlation coefficient of 0.77. The simplification results by eliminating the histogram from the procedure. Even though larger scatter is obvious (in comparison with Fig. 9), such a relationship implies that the average minimum temperature as obtained from infrared imagery can determine the rainy portion of the cloud for which a satellite ATI is associated, on an average. The elimination of cell 1A increases the correlation coefficient to .79. Conversion of the ATI's to rain volumes, as done previously, remains. Results from the application of this procedure to the 18 test cases are tabulated in column 4 of Table 4; and, when compared to column 2 (radar ATI rain volume, considered the true estimates), an average standard error, 1.67, is found.

As a by-product of the radar analysis, rain volumes were also determined by the Z-R optimized relationship (Smith *et al.*, 1975) and are given in column 5 of Table 4. Comparison is quite good with the products of the other three methods, except for Cell 1A. That confirms our hypothesis that the early elimination of cirrus debris from the calculation substantially reduced the rain volume estimates; in Table 4, columns 2 and 5, only radar data were considered, while in columns 3 and 4, satellite data were the basis of the calculations.

TABLE 4

Rain Volumes by Four Methods

Cell No	ATI Radar (kT)	Ave T _{Min} vs T _M and ATI (Sat) (kT)	Ave T _{Min} vs ATI Satellite (kT)	ZR Radar (kT)
1A	24,557	3,032	4,443	16,119
1B	5,847	1,029	6,298	4,082
E	6,826	1,331	5,478	6,831
X1	9,983	12,255	14,548	11,001
X2	7,017	3,253	24,267	1,027
A	3,668	9,600	14,934	4,268
C1	28,510	75,164	11,006	43,771
C2	744	1,284	2,015	1,599
C3	874	1,014	1,027	1,645
C4	702	<536	396	1,289
C5	11,788	6,376	1,673	12,477
C6	36	5.3	615	19
C7	3,159	4,965	1,075	3,550
C9	2,057	454	1,027	1,110
C10	661	<23	601	340
C11	239	65	574	181
D1	38,653	12,074	21,107	38,446
D2	18,371	7,875	17,523	17,649
Standard Error 0.74±0.40 1.67±3.69				

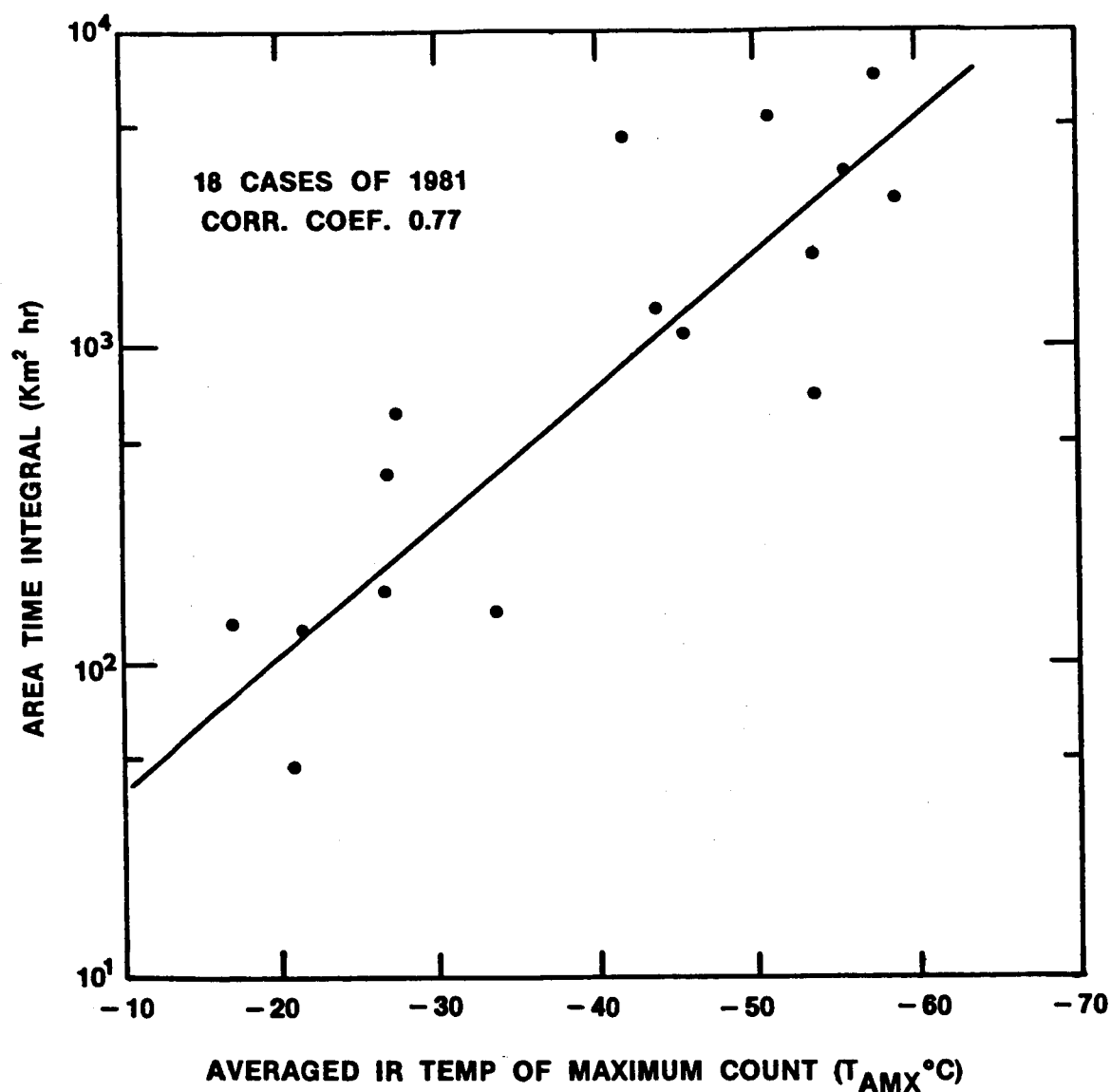


Fig. 12: Scatter and linear regression of ATI and average (over the cell duration) of IR minimum temperatures as determined by satellite imagery.

5. CONCLUDING REMARKS

This analysis of 18 convective clusters demonstrates that the extension of the ATI technique to the use of satellite data is possible. The differences of the internal structure of the radar reflectivity features (taken close to the cloud base), and of the satellite features (taken near the top of the cloud), give rise to differences in estimating rain volumes by delineating area; however, by focusing upon the area integrated over the lifetime of the storm, the investigation suggests that some of the errors produced by the differences in the cloud geometries as viewed by radar or satellite are minimized.

The results are good and future developments should consider data from different climatic regions and should allow for implementation of the technique in a general circulation model. Retrieved surface fields of temperatures (over the Northern Hemisphere, for instance) might be considered to adjust the linear regression described in Fig. 9.

Models describing the structure of radar reflectivities and minimum temperatures of infrared digital counts as a function of surface area and time are similar above given satellite and radar thresholds.

It is of crucial importance in this type of analysis to determine accurately the start and the end times of the convective events. The starting time can easily be determined when the first cluster's echo is visible in the radar data. Yet, the cirrus debris makes the definition of the decay portion or the end of the cluster as a convective entity from the satellite images difficult. This inconvenience can be overcome if the maximum development of the cluster is taken as the ending time of the analysis. The ATI technique also works if only the growing part of the cluster lifetime is considered (Doneaud *et al.*, 1984b). The maximum development of the cluster can be defined using radar data as the maximum echo height, the maximum reflectivity, or the maximum echo area >25 dBz. Satellite data definition of maximum development could be based on the maximum count value (i.e., the minimum temperature). Future investigations are anticipated to test such a procedure.

In some of the graphs presented (Figs. 4A-S and 5A-S), time lags between satellite and radar products as great as 30 min were observed. Maximum echo height, maximum reflectivity, and maximum echo area were found to occur before the IR temperature threshold matching echo areas >25 dBz and the minimum temperature of infrared maximum count.

In practice, the technique involves the use of two linear regressions and a histogram to estimate rain volumes. The first linear regression relating the IR minimum temperature averaged over

the cluster lifetime to the temperature matching the radar ATI (corr. coef. of .93) is used to delineate the rainy portion of the convective cloud area. The histogram relates the temperature matching the radar ATI to the ATI. The second linear regression estimates the total rain volume from the ATI.

The simplified procedure involves just two linear regressions: one relates the average IR minimum temperature direct to the satellite ATI (correlation coefficient .77), and the second relates the ATI to the rain volume. Application of this simplified procedure gave poorer results, as expected. Improvement may be possible by exercising more care in the definition of the satellite sector of interest. Further work is definitely indicated.

6. PAPERS PRESENTED AND PUBLISHED

Doneaud, A. A., J. R. Miller, Jr., L. R. Johnson, T. H. Vonder Haar and P. Laybe, 1984: An attempt to extend the ATI technique to estimate convective rain volumes using satellite data. Preprints 22nd Conf. Radar Meteor., Zurich, Switzerland, Amer. Meteor. Soc., 176-181.

_____, _____, _____, _____, and _____, 1985: The area-time-integral technique to estimate convective rain volumes over areas applied to satellite data - A preliminary investigation. Preprints 6th Conf. Hydrometeor., Indianapolis, IN, Amer. Meteor. Soc., 238-245.

_____, J. R. Miller, Jr., L. R. Johnson, T. H. Vonder Haar and P. Laybe, 1986: The area-time-integral technique to estimate convective rain volumes over areas applied to satellite data - A preliminary investigation. J. Climate Appl. Meteor., 26, 156-169.

_____, _____, and A. Makarau, 1986: A modified ATI technique for possible satellite applications. Preprints 23rd Conf. Radar Meteor., Snowmass, CO, Amer. Meteor. Soc., JP27-JP32.

Doneaud, A. A., L. R. Johnson, T. H. Vonder Haar, D. Reinke and P. Laybe, 1987: The area-time-integral technique applied to satellite data. [To be submitted to J. Climate Appl. Meteor.]

_____, A. Makarau and L. R. Johnson, 1987: A modified ATI technique for nowcasting convective rain volumes over areas. [Accepted by J. Climate Appl. Meteor.]

Johnson, L. R., A. A. Doneaud, T. H. Vonder Haar, D. Reinke and P. Laybe, 1987: The satellite area-time-integral technique to estimate rain volumes over areas. Preprints 7th Conf. Hydrometeor., 6-9 Oct 1987, Edmonton, Canada, Amer. Meteor. Soc., --.

7. REFERENCES

- Adler, R. J., and R. A. Mach, 1984: Thunderstorm cloud height-rainfall rate relations for use with satellite rainfall estimation techniques. J. Climate Appl. Meteor., 23, 280-296.
- Augustine, J. A., C. G. Griffith, W. L. Woodley and J. G. Meitin, 1981: Insights into errors of SMS-inferred GATE convective rainfall. J. Appl. Meteor., 20, 509-520.
- Austin, P. M., and R. A. Houze, Jr., 1972: Analysis of the structure of precipitation patterns in New England. J. Appl. Meteor., 11, 926-935.
- Barrett, E. C., and D. W. Martin, 1981: The Use of Satellite Data in the Rainfall Monitoring. Academic Press. 340 pp.
- Clark, J. D., 1983: The GOES Users Guide. NOAA NESDIS, Washington, DC. 156 pp.
- Doneaud, A. A., P. L. Smith, A. S. Dennis and S. Sengupta, 1981a: A simple method for estimating the convective rain volume over an area. Water Resources Res., 17, 1676-1682.
- _____, J. R. Miller, Jr., D. L. Priegnitz and T. Engel, 1981b: The role of mesoscale surface motions in the life of a convective storm in a dry continental climate. Proc. IAMAP-NOWCASTING Symposium, Hamburg, West Germany, 155-160. [Available from the European Space Agency, 8-10 rue Mario-Nikis, 75738 Paris 15, France]
- _____, S. Ionescu-Niscov, D. L. Priegnitz and P. L. Smith, 1984a: The area-time integral as an indicator for convective rain volumes. J. Climate Appl. Meteor., 23, 555-561.
- _____, _____, and J. R. Miller, Jr., 1984b: Convective rain rates and their evolution during storms in a semi-arid climate. Mon. Wea. Rev., 112, 1602-1612.
- _____, J. R. Miller, Jr., L. R. Johnson, T. H. Vonder Haar and P. Laybe, 1984c: An attempt to extend the ATI technique to estimate convective rain volumes using satellite data. Preprints 22nd Conf. Radar Meteor., Zurich, Switzerland, Amer. Meteor. Soc., 176-181.
- _____, _____, and L. R. Johnson, 1987: The area-time-integral technique to estimate convective rain volumes over areas applied to satellite data - A preliminary investigation. J. Climate Appl. Meteor., 26, 156-169.

- Fankhauser, J. C., G. M. Barnes, L. J. Miller and P. M. Roskowski, 1983: Photographic documentation of some distinctive cloud forms observed beneath a large cumulonimbus. Bull. Amer. Meteor. Soc., 64, 450-462.
- Griffith, C. G., W. L. Woodley, S. Browner, J. Teijeiro, M. Maier, D. W. Martin, J. Stout and S. N. Sikdar, 1976: Rainfall estimation from geosynchronous satellite imagery during daylight hours. NOAA Tech. Rep. ERL 356-WMP0 7, Boulder, CO. 106 pp.
- _____, _____, P. G. Grube, D. W. Martin, J. Stout and D. N. Sikdar, 1978: Rain estimation from geosynchronous satellite imagery. Visible and infrared studies. Mon. Wea. Rev., 106, 1153-1171.
- _____, J. A. Augustine and W. L. Woodley, 1981: Satellite rain estimation in the U.S. High Plains. J. Appl. Meteor., 20, 53-66.
- Laybe, P. V., 1983: An overview of the present and future uses of the CSU IRIS/DRSES. Dept. Atmos. Sci., Colorado State University, Fort Collins, CO.
- Lovejoy, S., and G. L. Austin, 1979: The sources of error in rain amount estimating schemes from GOES visible and IR satellite data. Mon. Wea. Rev., 107, 1048-1054.
- Minnis, P., and E. F. Harrison, 1984: Diurnal variability of regional cloud and clear-sky radiative parameters derived from GOES data. Part III: November 1978 radiative parameters. J. Climate Appl. Meteor., 23, 1032-1051.
- Negri, A. J., and R. F. Adler, 1981: Relation of satellite based thunderstorm intensity to radar estimated rainfall. J. Appl. Meteor., 20, 288-300.
- _____, _____, and P. J. Wetzel, 1984: Rain estimation from satellites: An examination of the Griffith-Woodley Technique. J. Climate Appl. Meteor., 23, 102-116.
- Rongzhang, W., J. A. Weinman and R. T. Chin, 1985: Determination of rainfall rates from GOES satellite images by a pattern recognition technique. J. Atmos. Ocean. Tech., 2, 314-330.
- Schroeder, M. J., and G. E. Klazura, 1978: Computer processing of digital radar data gathered during HIPLEX. J. Appl. Meteor., 17, 498-507.
- Scofield, C. A., and V. J. Oliver, 1977: A scheme for estimating convective rainfall from satellite imagery. NOAA Tech. Memo NESS 80. 47 pp.

- Smith, P. L., Jr., D. E. Cain and A. S. Dennis, 1975: Derivation of an R-Z relationship by computer optimization and its use in measuring daily areal rainfall. Preprints 16th Radar Meteor. Conf., Houston, TX, Amer. Meteor. Soc., 461-466.
- Super, A. B., and J. A. Heimbach, Jr., 1980: Rain gage network requirements from a simulated convective complex weather modification experiment. J. Appl. Meteor., 19, 1176-1183.
- Tsonis, A. A., and G. A. Isaac, 1985: On a new approach for instantaneous rain area delineation in the midlatitudes using GOES data. J. Climate Appl. Meteor., 24, 1208-1218.
- Woodley, W. L., C. G. Griffith, J. S. Griffin and S. C. Stromatt, 1980: The inference of GATE convective rainfall from SMS-1 imagery. J. Appl. Meteor., 19, 388-408.